

Chaotification in an internal-resonance-based electromagnetic vibration energy harvester

Jingyu Zhang (✉ d201780193@hust.edu.cn)

Huazhong University of Science and Technology <https://orcid.org/0000-0002-0985-2133>

Xuefeng Li

Huazhong University of Science and Technology

Renfu Li (✉ renfu.li@hust.edu.cn)

Huazhong University of Science and Technology

Research Article

Keywords: Internal resonance, Bistable nonlinearity, Double-jumping phenomenon, Bifurcation analysis, Basin-of-attraction

Posted Date: February 15th, 2021

DOI: <https://doi.org/10.21203/rs.3.rs-171092/v1>

License:   This work is licensed under a Creative Commons Attribution 4.0 International License.

[Read Full License](#)

Chaotification in an internal-resonance-based electromagnetic vibration energy harvester

Jingyu Zhang^{1,2*}, Xuefeng Li², Renfu Li^{2**}

1. School of Mechanical Science and Engineering, Huazhong University of Science and Technology, Wuhan, 430074, China

2. School of Aerospace Engineering, Huazhong University of Science and Technology, Wuhan, 430074, China

* Corresponding author, email: d201780193@hust.edu.cn

**Corresponding author, email: renfu.li@hust.edu.cn

ABSTRACT

This paper explores a 2:1 internal resonance of a bistable vibration energy harvester (BVEH) to enhance the harvesting performance. Two linear natural frequencies are tuned to meet the nearly commensurate ratio, i.e., 1:2. Thus, the 2:1 internal resonance could be activated when the first mode is directly excited under the same vibration frequency as the first linear natural frequency. The amplitude-frequency responses under small vibration amplitudes are obtained through the multi-scale method. The analytic results reveal the double-jumping characteristics, which could expand the bandwidth of the BVEH. Among them, an intriguing “flower pattern” amplitude-frequency curve is observed. Besides, the frequency spectrums are introduced to demonstrate the mode coupling and energy exchange between the first two modes. With small vibration amplitude, only intra-well responses could be obtained, and the energy exchange between modes obeys strict commensurate relation, i.e., 2:1. However, it does not obey the 2:1 ratio when the inter-well responses are activated, and the energy transfers to several low-frequency modes which results in a chaotic inter-well response. Afterward, the bifurcation diagrams and basin-of-attraction maps are explored by the numerical method to develop insights into the nonlinear responses of the BVEH. The results quantitatively prove the enhancement of the inter-well responses by internal resonance, and the chaotic inter-well response dominates the nonlinear behaviors.

Keywords: Internal resonance; Bistable nonlinearity; Double-jumping phenomenon; Bifurcation analysis; Basin-of-attraction

1 Introduction

Nonlinearity is becoming more attractive and ubiquitous in terms of the dynamic characteristics compared to linearity. Unlike the linear systems, which are strongly affected by the resonance, some nonlinear systems are known as the non-resonant structures, and their dynamic behaviors could be desirable even the excitation frequency is far away from the linear natural frequencies [1]. Thus, nonlinearity has been employed in the design of mechanical equipment that requires great kinetic energy, such as actuators [2], locomotion robots [3], energy harvesters [4], etc.

The vibration energy harvester (VEH) is an electromechanical device based on a linear or nonlinear oscillator, which could convert ambient wasted vibration energy into electrical power, and the harvesting efficiency is highly dependent on the oscillator’s kinetic energy. In the past two decades, energy harvesting has attracted much attention due to its convenience and cleanness, and it is an effective solution to solve the power supply problems of wireless self-sustained electrical electronics [5]. In recent researches, scholars have found that the VEHs based on nonlinearity outperform those based on linearity in terms of output displacement and harvesting efficiency. Fully utilizing the nonlinear characteristics of a structure could

greatly improve the harvesting performance. Among them, the bistable nonlinearity draws much attention, and the snap-through motion could significantly improve the oscillator's kinetic energy, which contributes to high efficiency in transducing vibration energy into electrical power. Yang et al. [6] proposed a double-beam piezo-magneto-elastic wind energy harvester which consisted of two piezoelectric beams, and both beams were supported by a prism-like bluff embedded with a permanent magnet. The bistability was induced by the magnetic repulsion force, and the harvesting power was enhanced by the bistable nonlinearity. Furthermore, employing an additional oscillator or dynamic magnifier could transfer a 1-DOF VEH to multi-DOF VEH to obtain multi-modal characteristic, which has been proven to be an effective solution to broaden the bandwidth [7-9]. Harne et al. [10] proposed an inclined-spring-based bistable energy harvester attached to an additional linear oscillator for harvesting enhancement. They found the additional DOF of the linear oscillator was an effective approach to enhance the VEH harvesting performance and robustness.

Internal resonance, which is one of the unique phenomena in the multi-DOF nonlinear dynamics, occurs when the linear natural frequencies of the first two vibration modes are in commensurate or nearly commensurate ratio, i.e., 1:2 or 1:3, etc. There are several significant investigations on the internal resonance: fluid-conveying pipe [11], marine riser [12], arch beams [13], composite plates [14], nanoscale rods [15], rotor systems [16], magnetic resonance force microscopy [17], and the unique phenomenon such as mode interaction was revealed by Galerkin truncation, multi-scale method, harmonic balance method, etc. Nonlinear behaviors such as bifurcation and chaos were detected as well. Wang et al. [18] investigated the 1:3 internal resonance of two coupled micro-resonators, and the frequency locking phenomenon was discovered for the first time once the coupling strength exceeded a critical value. Christopher and Jae [19] reported the multi-stable energy exchange between modes of a crystal plate, and the new insight into the complex interactions was presented by a mixed analytical-numerical method.

The internal resonance characteristics provide mode coupling and energy exchange [20]. The amplitude-frequency response of an internal-resonance-based VEH bends to both directions which could broaden the bandwidth [21,22]. As a result, internal resonance has been explored as a possible control mechanism to enhance the harvesting efficiency for the VEHs [23-28].

Recently, Chen and Jiang [29] explored the internal resonance as a possible approach to enhance the vibration energy harvesting efficiency. The amplitude-frequency responses were derived through the multi-scale method, and two peaks bending to both the left and right directions were obtained. The averaged power was calculated, which outperformed the linear energy harvester under the same conditions. Xiong et al. [30] induced the unique internal resonance in a nonlinear VEH to pursue wider bandwidth. The nonlinearity was introduced by the magnetic interaction, and an additional oscillator was attached to a conventional 1-DOF VEH. Thus, the internal resonance could be induced when the first two linear frequencies were tuned to be commensurable ratio. Yang and Towfighian [31] presented a broadband internal-resonance-based energy harvester, and the nonlinearity was induced by the magnetic force. The results showed that the bandwidth of the proposed energy harvester was enlarged by 110% compared to the linear system when the internal resonance happened. Combining the nonlinear energy sink and the internal resonance, Hou et al. [32] proposed a 3:1 internal resonance system as an enhancement approach for energy harvesting. The results demonstrated the feasibility of the internal resonance characteristics. In Ref [33], Lan et al. found the dynamic instability a determinant for the internal resonance and the mode coupling. And the internal resonance could transfer the excitation energy between the first and the second modes, which could bring a large output power. Nie et al. [34] exploited the 1:2 internal resonance in an L-shaped piezoelectric energy harvester, several dynamic responses such as periodic responses, quasi-periodic

responses, and chaotic responses were observed. They found the internal resonance enabled the energy harvester to harvest ambient energy more efficiently over a broader bandwidth.

Inspired by the above researches, this paper investigates the 2:1 internal resonance of a 2-DOF bistable VEH (BVEH) to pursue broadband harvesting and intriguing nonlinear phenomena. The bistable nonlinearity is introduced by an one DOF inclined-spring-based bistable oscillator, and the second DOF is introduced by an auxiliary oscillator which could operate as an elastic boundary of the inclined-spring-based oscillator. The two DOFs intersect vertically, which could bring strong mode interaction and energy exchange. Under small vibration excitation amplitude, the double-jumping phenomenon manifests, and the bandwidth is enlarged. The energy exchange obeys strict commensurate relation. With the increase of the vibration amplitude, large-amplitude inter-well responses occur and the harvesting efficiency could be improved. The basin-of-attraction map is presented to demonstrate that the internal resonance does enhance the occurring probability of exhibiting inter-well responses, and the chaos is dominant.

2 Internal-resonance-based BVEH

2.1 Governing equation

Figure. 1 presents the schematic diagram of the BVEH. The BVEH combines with an inclined-spring-based bistable oscillator, an auxiliary oscillator, a linear track winded by coils, and the coils are connected with an electrical resistor R . The bistable oscillator has an embedded magnet mass (m_1) and an inclined spring whose stiffness and undeformed length are k_1 and L_1 , respectively. The auxiliary oscillator comprises a linear spring with stiffness k_2 and undeformed length L_2 , a linear damper c_2 , and an auxiliary mass block m_2 . One end of the inclined spring is bonded on m_1 , while the other end is connected to the auxiliary oscillator. There are two positions for the m_2 needed to be emphasized. The first one is the gray translucent position where k_2 is undeformed, and d is the vertical displacement from the top of m_1 to the bottom of the gray translucent m_2 position. The second one is the initial equilibrium position of m_2 which is the yellow block in the vertical direction in figure 1. m_1 slides on the linear track with a linear damping constant c_1 , and the current could be obtained by cutting the magnetic field. When the BVEH is exposed to an acceleration vibration excitation $\ddot{Z} = -p\cos(\Omega t)$, the governing equations of the BVEH could be expressed by

$$m_1(\ddot{x} + \ddot{Z}) + c_1\dot{x} + k_1x \left[1 - \frac{L_1}{\sqrt{(x^2 + (d-y)^2)}} \right] + \Gamma I = 0 \quad (1a)$$

$$m_2\ddot{y} + c_2\dot{y} + k_2y + k_1(y - d) \left(1 - \frac{L_1}{\sqrt{(x^2 + (d-y)^2)}} \right) - m_2g = 0 \quad (1b)$$

$$L_e\dot{I} + R_eI - \Gamma\dot{x} = 0 \quad (1c)$$

where x represents the relatively horizontal displacement from m_1 to the centerline, y is the variation of L_2 (relative displacement of m_2 to the position where k_2 is undeformed), g is the gravitational acceleration, p and Ω are the acceleration vibration excitation amplitude and frequency, respectively. I is the current flow through resistor R_e , L_e is the electromagnetic harvester inductance, Γ is the electromagnetic coupling constant, and the operator $(\dot{})$ is the derivative with respect to time t .

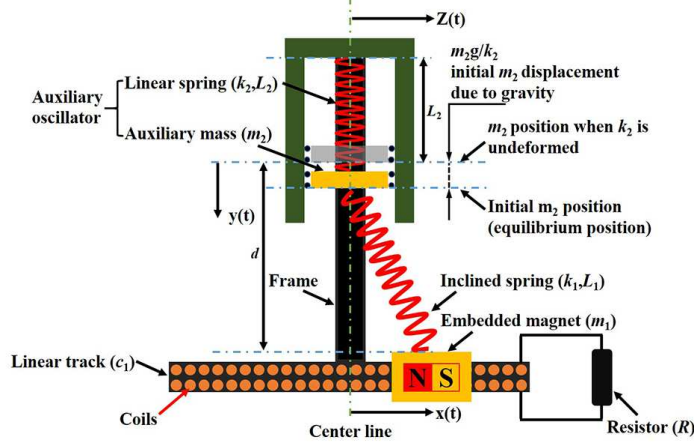


Fig. 1. Schematic diagram of the BVEH

2.2 Linear natural frequencies and modes

The static equilibria of the BVEH under the nonlinear restoring force could be obtained by letting the time derivatives to zero, and the satisfy the algebraic equations

$$k_1 x \left[1 - \frac{L_1}{\sqrt{(x^2 + (d-y)^2)}} \right] = 0 \quad (2a)$$

$$k_2 y + k_1 (y - d) \left(1 - \frac{L_1}{\sqrt{(x^2 + (d-y)^2)}} \right) - m_2 g = 0 \quad (2b)$$

three static equilibrium positions could be obtained, i.e., $(0, 0, (m_2 g - k_1(L_1 - d))/(k_1 + k_2), 0)$ and $(\pm \sqrt{L_1^2 - (d - m_2 g/k_2)^2}, 0, m_2 g/k_2, 0)$. Besides, $x_s = \pm \sqrt{L_1^2 - (d - m_2 g/k_2)^2}$ and $y_s = m_2 g/k_2$ are the two stable static equilibrium displacements of m_1 and m_2 , which are symmetrical about the centerline, i.e., bistability [2,35]. Under small vibration amplitude, the BVEH will exhibit the small-amplitude intra-well oscillations. Introducing the relative displacements from (x_s, y_s)

$$X = x - x_s, Y = y - y_s \quad (3)$$

Eq. (1) becomes

$$m_1 (\ddot{X} + \ddot{Z}) + c_1 \dot{X} + k_1 (X + b) \left[1 - \frac{L_1}{\sqrt{((X+b)^2 + (D-Y)^2)}} \right] + \Gamma I = 0 \quad (4a)$$

$$m_2 \ddot{Y} + c_2 \dot{Y} + k_2 Y - k_1 (D - y_s) \left[1 - \frac{L_1}{\sqrt{((X+x_s)^2 + (D-y_s)^2)}} \right] = 0 \quad (4b)$$

$$L_e \dot{I} + R_e I - \Gamma \dot{X} = 0 \quad (4c)$$

where $D = d - y_s$ is defined. By multivariate Taylor series expansion at $(X = 0, Y = 0)$ and keeping the quadratic terms, the Eq. (4) is rewritten as

$$m_1 \ddot{X} + c_1 \dot{X} + K_1 X - K_2 Y + Q_1 X^2 + Q_2 XY + Q_3 Y^2 = m_1 p \cos(\Omega t) \quad (5a)$$

$$m_2 \ddot{Y} + c_2 \dot{Y} - K_3 X + K_4 Y + Q_4 X^2 + Q_5 XY + Q_6 Y^2 = 0 \quad (5b)$$

$$L_e \dot{I} + R_e I - \Gamma \dot{X} = 0 \quad (5c)$$

where

$K_1 = \frac{k_1 x_s^2}{L_1^2}$, $K_2 = \frac{k_1 x_s D}{L_1^2}$, $K_3 = \frac{k_1 x_s D}{L_1^2}$, $K_4 = k_2 + \frac{k_1 D^2}{L_1^2}$, $Q_1 = \frac{3k_1 x_s D^2}{2L_1^4}$, $Q_2 = -\frac{k_1 D(D^2 - 2x_s^2)}{L_1^4}$, $Q_3 = -\frac{k_1 x_s(2D^2 - x_s^2)}{2L_1^4}$, $Q_4 = -\frac{k_1 D(D^2 - 2x_s^2)}{2L_1^4}$, $Q_5 = -\frac{k_1 x_s(2D^2 - x_s^2)}{L_1^4}$, $Q_6 = -\frac{3k_1 D x_s^2}{2L_1^4}$. In addition, as the quadratic terms dominate the nonlinearity of Eq. (5), thus, the 2:1 internal resonance could be activated when the

BVEH is appropriately tuned. Considering the undamped free vibration, the first two linear natural frequencies and the corresponding two modes of the BVEH are

$$\omega_{n(1,2)}^2 = \frac{K_1/m_1 + K_4/m_2}{2} \mp \sqrt{\left(\frac{K_1/m_1 - K_4/m_2}{2}\right)^2 + \frac{K_2 K_3}{m_1 m_2}} \quad (6)$$

$$\begin{pmatrix} 1 \\ P_n \end{pmatrix} = \begin{pmatrix} 1 \\ \frac{K_1 - m_1 \omega_n^2}{K_2} \end{pmatrix}, (n = 1, 2) \quad (7)$$

2.3 Model validation using the MSC Adams software

The experimental prototype of the BVEH, which does not be tuned to have internal resonance characteristics, is presented in the appendix. The accuracy of the governing equations, i.e., Eq. (1), is experimentally validated. Besides, the MSC Adams software is also employed to validate the mathematical model of the BVEH which is tuned to have internal resonance characteristics. The 3D virtual prototype is established shown in Figure 2 and the simulation parameters are listed in Table 1.

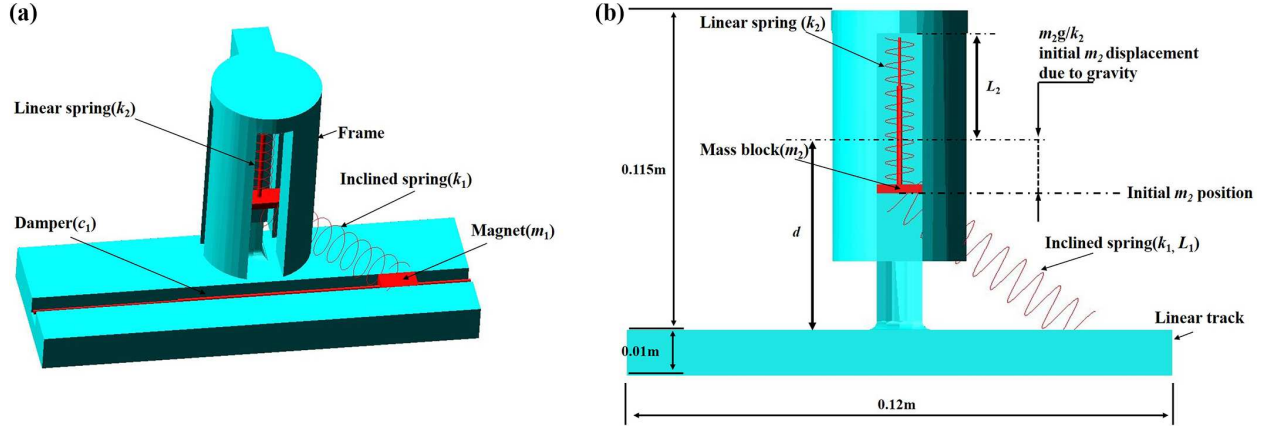


Fig. 2. The 3D virtual prototype of the BVEH in Adams software. (a) Isometric graph; (b) planar graph.

Table 1 The simulation parameters

parameters	values
m_1 (kg)	0.1
m_2 (kg)	0.1
L_1 (m)	0.05
L_2 (m)	0.0125
d (m)	0.0495
k_1 (N/m)	56
k_2 (N/m)	50
c_1 (N/(m/s))	0.001
c_2 (N/(m/s))	0.002

Two time trajectories are presented in figure 3 to validate the accuracy of the governing equations. Two different vibration amplitudes are employed, the first one is a small amplitude with $p = 0.01\text{m/s}^2$, the second one uses a larger amplitude with $p = 10\text{m/s}^2$. $c_1 = 0.001\text{Ns/m}$, $c_2 = 0.002\text{Ns/m}$, and $\Omega = 3\text{Hz}$ are set as well. It is seen that the two results obtained by different methods match well. In figure 3(a), only the low-efficiency intra-well responses are obtained when vibration amplitudes are small. With a larger amplitude, the large-amplitude inter-well responses could be activated, as shown in figure 3(b). In general,

the accuracy of the mathematical model is validated, and the theoretical analyses of this paper are based on the governing equations.

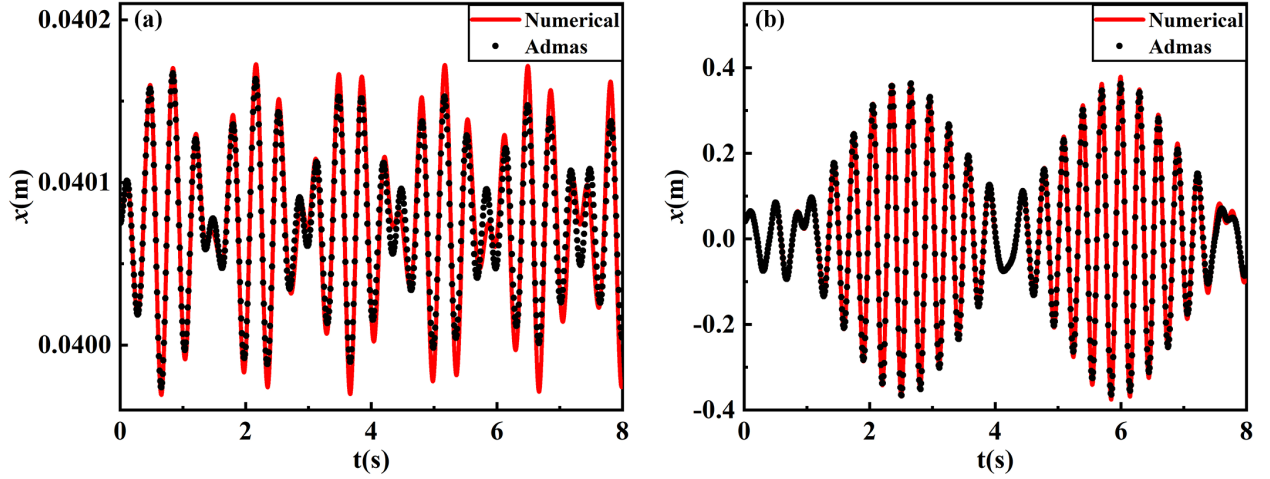


Fig. 3 Comparison between the numerical method and the Adams. (a) $p = 0.01\text{m/s}^2$; (b) $p = 10\text{m/s}^2$.

3 Amplitude–Frequency Response under small vibration amplitude

3.1 Multi-scale method

Introduce two new modal coordinates q_1 and q_2 , the X and Y could be expressed as

$$\begin{bmatrix} X \\ Y \end{bmatrix} = q_1 \begin{bmatrix} 1 \\ P_1 \end{bmatrix} + q_2 \begin{bmatrix} 1 \\ P_2 \end{bmatrix} \quad (8)$$

Substituting Eq. (8) into Eq. (5), and the linear parts of Eq. (5) are decoupled in the modal coordinates using the orthogonality of modes

$$\ddot{q}_1 + \omega_1^2 q_1 = -\zeta_{11}\dot{q}_1 - \zeta_{12}\dot{q}_2 + G_1 \cos(2\pi\Omega t) - (\Psi_1(q_1 + q_2)^2 + \Theta_1(q_1 + q_2)(P_1 q_1 + P_2 q_2) + Y_1(P_1 q_1 + P_2 q_2)^2 + v_1 I) \quad (9a)$$

$$\ddot{q}_2 + \omega_2^2 q_2 = -\zeta_{21}\dot{q}_1 - \zeta_{22}\dot{q}_2 + G_2 \cos(2\pi\Omega t) - (\Psi_2(q_1 + q_2)^2 + \Theta_2(q_1 + q_2)(P_1 q_1 + P_2 q_2) + Y_2(P_1 q_1 + P_2 q_2)^2 + v_2 I) \quad (9b)$$

$$L_e \dot{I} + R_e I - \Gamma(\dot{q}_1 + \dot{q}_2) = 0 \quad (9c)$$

Where $M_j = m_1 + P_j^2 m_2$, $\zeta_{jn} = \frac{c_1 + P_j c_2 P_n}{M_j}$, $G_j = \frac{m_1 p}{M_j}$, $\Psi_j = \frac{Q_1 + P_j Q_4}{M_j}$, $\Theta_j = \frac{Q_2 + P_j Q_5}{M_j}$, $Y_j = \frac{Q_3 + P_j Q_6}{M_j}$, $v_j = \frac{\Gamma}{M_j}$ ($j, n = 1, 2$). (10)

Small bookkeeping parameter ε is introduced to characterize the small vibration amplitude, the small displacement amplitude, the small current amplitude, the small damping, and the small electromagnetic coupling constant. Besides, the secular terms generated by the quadratic nonlinearities appear in the order ε^2 , thus, rescale the coefficients as

$$G_j \leftrightarrow \varepsilon^2 G_j, q_j \leftrightarrow \varepsilon q_j, \zeta_j \leftrightarrow \varepsilon \zeta_j, v_j \leftrightarrow \varepsilon v_j, I \leftrightarrow \varepsilon I. (j = 1, 2) \quad (11)$$

The rescaled governing equations become

$$\ddot{q}_1 + \omega_1^2 q_1 = \varepsilon[-\zeta_{11}\dot{q}_1 - \zeta_{12}\dot{q}_2 + G_1 \cos(2\pi\Omega t) - (\Psi_1(q_1 + q_2)^2 + \Theta_1(q_1 + q_2)(P_1 q_1 + P_2 q_2) + Y_1(P_1 q_1 + P_2 q_2)^2 + v_1 I)] \quad (12a)$$

$$\ddot{q}_2 + \omega_2^2 q_2 = \varepsilon[-\zeta_{21}\dot{q}_1 - \zeta_{22}\dot{q}_2 + G_2 \cos(2\pi\Omega t) - (\Psi_2(q_1 + q_2)^2 + \Theta_2(q_1 + q_2)(P_1 q_1 + P_2 q_2) + Y_2(P_1 q_1 + P_2 q_2)^2 + v_2 I)] \quad (12b)$$

$$L_e \dot{I} + R_e I - \Gamma(q_1 + q_2) = 0 \quad (12c)$$

The right hand of the Eq. (12) defines a nonlinear system dominated by the quadratic terms, thus, the 2:1 internal resonance could be activated when $\omega_2 = 2\omega_1$. Define the fast and slow time scales $T_0 = t$, and $T_1 = \varepsilon t$. The multi-scale method assumes the solutions to Eq. (12) to be

$$q_1(t, \varepsilon) = q_{10}(T_0, T_1) + \varepsilon q_{11}(T_0, T_1) + \dots \quad (13a)$$

$$q_2(t, \varepsilon) = q_{20}(T_0, T_1) + \varepsilon q_{21}(T_0, T_1) + \dots \quad (13b)$$

$$I = I_0(T_0, T_1) + \varepsilon I_1(T_0, T_1) + \dots \quad (13c)$$

The derivatives with respect to the old timescale t are changed to

$$\frac{d}{dt} = D_0 + \varepsilon D_1 + \dots \quad (14a)$$

$$\frac{d^2}{dt^2} = (D_0 + \varepsilon D_1 + \dots)^2 \quad (14b)$$

where D_j ($j = 1, 2, \dots$) represents the partial differential operator $\partial/\partial T_n$ ($n = 0, 2, \dots$). Substituting Eq. (13) and (14) into Eq. (12), and equating coefficients of ε^0 and ε^1 lead to

Order ε^0

$$D_0^2 q_{10} + \omega_1^2 q_{10} = 0 \quad (15a)$$

$$D_0^2 q_{20} + \omega_2^2 q_{20} = 0 \quad (15b)$$

$$L_e D_0 I_0 + R_e I_0 = \Gamma(D_0 q_{10} + D_0 q_{20}) \quad (15c)$$

Order ε^1

$$D_0^2 q_{11} + \omega_1^2 q_{11} = G_1 \cos(2\pi\Omega T_0) - 2D_0 D_1 q_{10} - \zeta_{11} D_0 q_{10} - \zeta_{12} D_0 q_{20} - Y_1 (P_1^2 q_{10}^2 + 2P_1 P_2 q_{10} q_{20} + P_2^2 q_{20}^2) - \Theta_1 (P_1 q_{10}^2 + P_1 q_{10} q_{20} + P_2 q_{10} q_{20} + P_2 q_{20}^2) - \Psi_1 (q_{10}^2 + 2q_{10} q_{20} + q_{20}^2) - v_1 I_0 \quad (16a)$$

$$D_0^2 q_{21} + \omega_2^2 q_{21} = G_2 \cos(2\pi\Omega T_0) - 2D_0 D_1 q_{20} - \zeta_{21} D_0 q_{10} - \zeta_{22} D_0 q_{20} - Y_2 (P_1^2 q_{10}^2 + 2P_1 P_2 q_{10} q_{20} + P_2^2 q_{20}^2) - \Theta_2 (P_1 q_{10}^2 + P_1 q_{10} q_{20} + P_2 q_{10} q_{20} + P_2 q_{20}^2) - \Psi_2 (q_{10}^2 + 2q_{10} q_{20} + q_{20}^2) - v_2 I_0 \quad (16b)$$

$$L_e D_0 I_1 + R_e I_1 = -L_e D_1 I_0 + \Gamma(D_0 q_{11} + D_0 q_{21}) + \Gamma(D_1 q_{10} + D_1 q_{20}) \quad (16c)$$

The solution of Eq. (15) in the complex form could be expressed as

$$q_{10} = A_1(T_1) e^{i\omega_1 T_0} + \overline{A_1}(T_1) e^{-i\omega_1 T_0} \quad (17a)$$

$$q_{20} = A_2(T_1) e^{i\omega_2 T_0} + \overline{A_2}(T_1) e^{-i\omega_2 T_0} \quad (17b)$$

$$I_0 = \frac{i\omega_1 \Gamma A_1(T_1)}{R_e + i\omega_1 L_e} e^{i\omega_1 T_0} + \frac{i\omega_2 \Gamma A_2(T_1)}{R_e + i\omega_2 L_e} e^{i\omega_2 T_0} + B(T_1) e^{-\frac{R_e T_0}{L_e}} + cc \quad (17c)$$

where $A_j(T_1)$ ($j = 1, 2$) and $B(T_1)$ are undetermined complex functions, and $\overline{A_j}(T_1)$ ($j = 1, 2$) are the complex conjugate of the $A_j(T_1)$. Substituting Eq. (17) into Eq. (16) yields

$$D_0^2 q_{11} + \omega_1^2 q_{11} = -2 \left(\left(\frac{P_1 + P_2}{2} \right) \Theta_1 + Y_1 P_1 P_2 + \Psi_1 \right) \overline{A_1} A_2 e^{i(\omega_2 - \omega_1) T_0} - 2 \left(\left(\frac{P_1 + P_2}{2} \right) \Theta_1 + Y_1 P_1 P_2 + \Psi_1 \right) A_1 A_2 e^{i(\omega_2 + \omega_1) T_0} - (Y_1 P_1^2 + \Theta_1 P_1 + \Psi_1) A_1^2 e^{i2\omega_1 T_0} - (Y_1 P_2^2 + \Theta_1 P_2 + \Psi_1) A_2^2 e^{i2\omega_2 T_0} - i\omega_1 \left(\zeta_{11} A_1 + 2D_1 A_1 + \frac{v_1 \Gamma A_1(T_1)}{R_e + i\omega_1 L_e} \right) e^{i\omega_1 T_0} - i\omega_2 \left(\zeta_{12} A_2 + \frac{v_1 \Gamma A_2(T_1)}{R_e + i\omega_2 L_e} \right) e^{i\omega_2 T_0} - (Y_1 P_1^2 + \Theta_1 P_1 + \Psi_1) A_1 \overline{A_1} - (Y_1 P_2^2 + \Theta_1 P_2 + \Psi_1) A_2 \overline{A_2} + \frac{G_1}{2} e^{i\Omega T_0} - v_1 B(T_1) e^{-\frac{R_e T_0}{L_e}} + cc \quad (18a)$$

$$D_0^2 q_{21} + \omega_2^2 q_{21} = -2 \left(\left(\frac{P_1 + P_2}{2} \right) \Theta_2 + Y_2 P_1 P_2 + \Psi_2 \right) \overline{A_1} A_2 e^{i(\omega_2 - \omega_1) T_0} - 2 \left(\left(\frac{P_1 + P_2}{2} \right) \Theta_2 + Y_2 P_1 P_2 + \Psi_2 \right) A_1 A_2 e^{i(\omega_2 + \omega_1) T_0} - (Y_2 P_1^2 + \Theta_2 P_1 + \Psi_2) A_1^2 e^{i2\omega_1 T_0} - (Y_2 P_2^2 + \Theta_2 P_2 + \Psi_2) A_2^2 e^{i2\omega_2 T_0} -$$

$$i\omega_2 \left(\zeta_2 A_2 + 2D_1 A_2 + \frac{v_2 \Gamma A_2(T_1)}{R_e + i\omega_2 L_e} \right) e^{i\omega_2 T_0} - i\omega_1 \left(\zeta_{21} A_1 + \frac{v_2 \Gamma A_1(T_1)}{R_e + i\omega_1 L_e} \right) e^{i\omega_1 T_0} - (\Upsilon_2 P_1^2 + \Theta_2 P_1 + \Psi_2) A_1 \overline{A_1} - (\Upsilon_2 P_2^2 + \Theta_2 P_2 + \Psi_2) A_2 \overline{A_2} + \frac{G_2}{2} e^{i\Omega T_0} + cc \quad (18b)$$

$$D_0 I_1 + \frac{R_e}{L_e} I_1 = - \left(\frac{i\omega_1 \Gamma D_1 A_1(T_1)}{R_e + i\omega_1 L_e} e^{i\omega_1 T_0} + \frac{i\omega_2 \Gamma D_1 A_2(T_1)}{R_e + i\omega_2 L_e} e^{i\omega_2 T_0} + D_1 B(T_1) e^{-\frac{R_e T_0}{L_e}} \right) + \frac{\Gamma}{L_e} (D_0 q_{11} + D_1 A_1(T_1) e^{i\omega_1 T_0}) + \frac{\Gamma}{L_e} (D_0 q_{21} + D_1 A_2(T_1) e^{i\omega_2 T_0}) + cc \quad (18c)$$

where cc stands for the complex conjugate of the preceding terms.

3.2 First primary resonance under small vibration amplitude

The detuning parameters σ_0 and σ_1 are introduced to describe the nearness of the vibration frequency Ω to ω_1 and ω_2 to $2\omega_1$, respectively. Thus, the frequency relations for the 2:1 internal resonance when the first linear frequency is directly excited are described by

$$\Omega = \omega_1 + \varepsilon \sigma_0, \quad \omega_2 = 2\omega_1 + \varepsilon \sigma_1 \quad (19)$$

Substituting Eq. (19) into Eq. (18) and eliminating the secular terms yield

$$D_1 A_1 = \Xi_{11} A_1 + \Xi_{12} \overline{A_1} A_2 e^{i\sigma_1 T_1} + \Xi_{13} I_1 e^{i\sigma_0 T_1} \quad (20a)$$

$$D_1 A_2 = \Xi_{21} A_2 + \Xi_{22} A_1^2 e^{-i\sigma_1 T_1} \quad (20b)$$

where

$$\Xi_{11} = -\frac{\zeta_{11}}{2} - \frac{v_1 \Gamma}{2(R_e + i\omega_1 L_e)}, \quad \Xi_{12} = \frac{-\left(\frac{P_1 + P_2}{2}\right) \Theta_1 + \Upsilon_1 P_1 P_2 + \Psi_1}{i\omega_1}, \quad \Xi_{13} = \frac{1}{4\omega_1 i}, \quad \Xi_{21} = -\frac{\zeta_{22}}{2} - \frac{v_2 \Gamma}{2(R_e + i\omega_2 L_e)}, \quad \Xi_{22} = \frac{-(\Upsilon_2 P_1^2 + \Theta_2 P_1 + \Psi_2)}{2i\omega_2}. \quad (21)$$

The complex functions $A_j(T_1)$ ($j = 1, 2$) could be expressed in the polar form

$$A_j(T_1) = \frac{1}{2} \Lambda_j(T_1) e^{i\theta_j(T_1)} \quad (22)$$

where Λ_j and θ_j are real functions with respect to T_1 . Substituting Eq. (22) into Eq. (20) and separating the real and the imaginary parts yield

$$D_1 \Lambda_1 = \text{Re}(\Xi_{11}) \Lambda_1 + \frac{1}{2} \Lambda_1 \Lambda_2 (\text{Re}(\Xi_{12}) \cos \eta_1 - \text{Im}(\Xi_{12}) \sin \eta_1) + 2I_1 (\text{Re}(\Xi_{13}) \cos \eta_2 - \text{Im}(\Xi_{13}) \sin \eta_2) \quad (23a)$$

$$D_1 \Lambda_2 = \text{Re}(\Xi_{21}) \Lambda_2 + \frac{1}{2} \Lambda_1^2 (\text{Re}(\Xi_{22}) \cos \eta_1 + \text{Im}(\Xi_{22}) \sin \eta_1) \quad (23b)$$

$$D_1 \eta_1 = \sigma_1 + \text{Im}(\Xi_{21}) - 2\text{Im}(\Xi_{11}) + \frac{1}{2} \frac{\Lambda_1^2}{\Lambda_2} (\text{Im}(\Xi_{22}) \cos \eta_1 - \text{Re}(\Xi_{22}) \sin \eta_1) - \Lambda_2 (\text{Im}(\Xi_{12}) \cos \eta_1 + \text{Re}(\Xi_{12}) \sin \eta_1) - \frac{4I_1}{\Lambda_1} (\text{Im}(\Xi_{13}) \cos \eta_2 + \text{Re}(\Xi_{13}) \sin \eta_2) \quad (23c)$$

$$D_1 \eta_2 = \sigma_0 - \text{Im}(\Xi_{11}) - \frac{1}{2} \Lambda_2 (\text{Im}(\Xi_{12}) \cos \eta_1 + \text{Re}(\Xi_{12}) \sin \eta_1) - \frac{2I_1}{\Lambda_1} (\text{Im}(\Xi_{13}) \cos \eta_2 + \text{Re}(\Xi_{13}) \sin \eta_2) \quad (23d)$$

where

$$\eta_1 = \theta_2 - 2\theta_1 + \sigma_1 T_1, \quad \eta_2 = \sigma_0 T_1 - \theta_1 \quad (24)$$

For the steady-state response, Λ_j and η_j ($j = 1, 2$) should be independent of T_1 . Therefore

$$\text{Re}(\Xi_{11}) \Lambda_1 + \frac{1}{2} \Lambda_1 \Lambda_2 (\text{Re}(\Xi_{12}) \cos \eta_1 - \text{Im}(\Xi_{12}) \sin \eta_1) + 2I_1 (\text{Re}(\Xi_{13}) \cos \eta_2 - \text{Im}(\Xi_{13}) \sin \eta_2) = 0 \quad (25a)$$

$$\text{Re}(\Xi_{21}) \Lambda_2 + \frac{1}{2} \Lambda_1^2 (\text{Re}(\Xi_{22}) \cos \eta_1 + \text{Im}(\Xi_{22}) \sin \eta_1) = 0 \quad (25b)$$

$$\sigma_1 + \text{Im}(\Xi_{21}) - 2\text{Im}(\Xi_{11}) + \frac{1}{2} \frac{\Lambda_1^2}{\Lambda_2} (\text{Im}(\Xi_{22})\cos\eta_1 - \text{Re}(\Xi_{22})\sin\eta_1) - \Lambda_2 (\text{Im}(\Xi_{12})\cos\eta_1 + \text{Re}(\Xi_{12})\sin\eta_1) - \frac{4I_1}{\Lambda_1} (\text{Im}(\Xi_{13})\cos\eta_2 + \text{Re}(\Xi_{13})\sin\eta_2) = 0 \quad (25c)$$

$$\sigma_0 - \text{Im}(\Xi_{11}) - \frac{1}{2} \Lambda_2 (\text{Im}(\Xi_{12})\cos\eta_1 + \text{Re}(\Xi_{12})\sin\eta_1) - \frac{2I_1}{\Lambda_1} (\text{Im}(\Xi_{13})\cos\eta_2 + \text{Re}(\Xi_{13})\sin\eta_2) = 0 \quad (25d)$$

Eliminating η_1 , η_2 , and Λ_1 from Eq. (25), the amplitude-frequency response relationship in the first mode is obtained

$$\Gamma_1 \Lambda_1^6 + \Gamma_2 \Lambda_1^4 + \Gamma_3 \Lambda_1^2 + \Gamma_4 = 0 \quad (26)$$

where

$$\Gamma_1 = \frac{\text{Im}(\Xi_{22})^2 \text{Im}(\Xi_{12})^2}{16(\text{Re}(\Xi_{21})^2 + (2\sigma_0 - \sigma_1 - \text{Im}(\Xi_{21}))^2)} \quad (27a)$$

$$\Gamma_2 = \frac{\text{Im}(\Xi_{22})\text{Im}(\Xi_{12})(\text{Re}(\Xi_{11})\text{Re}(\Xi_{21}) - (2\sigma_0 - \sigma_1 - \text{Im}(\Xi_{21}))(\sigma_0 - \text{Im}(\Xi_{11})))}{2(\text{Re}(\Xi_{21})^2 + (2\sigma_0 - \sigma_1 - \text{Im}(\Xi_{21}))^2)} \quad (27b)$$

$$\Gamma_3 = \text{Re}(\Xi_{11})^2 + (\sigma_0 - \text{Im}(\Xi_{11}))^2 \quad (27c)$$

$$\Gamma_4 = -4G_1^2 \text{Im}(\Xi_{13})^2 \quad (27d)$$

The amplitude-frequency response relationship in the second mode is

$$\Lambda_2^2 = \frac{\Lambda_1^4 \text{Im}(\Xi_{22})^2}{4(\text{Re}(\Xi_{21})^2 + (2\sigma_0 - \sigma_1 - \text{Im}(\Xi_{21}))^2)} \quad (28)$$

According to Eq. (8) and Eq. (13), the displacement (X) and the current (I) amplitude could be expressed as

$$X = \Lambda_1 \cos(\omega_1 T_0 + \theta_1) + \Lambda_2 \cos(\omega_2 T_0 + \theta_2) \quad (29)$$

$$I = \frac{\omega_1 \Gamma \Lambda_1}{\sqrt{R_e^2 + \omega_1^2 L_e^2}} \cos(\omega_1 T_0 + \theta_1 + \beta_1) + \frac{\omega_2 \Gamma \Lambda_2}{\sqrt{R_e^2 + \omega_2^2 L_e^2}} \cos(\omega_2 T_0 + \theta_2 + \beta_2) \quad (30)$$

where $\beta_n = \arctan(R_e/(\omega_n L_e))$.

3.3 Stability analysis

The stability of the above steady-state responses could be determined via the Lyapunov theory [35]. The assumed polar form solution is not suitable for the stability analysis due to the presence of $\Lambda_1 D_1 \Lambda_1$ and $\Lambda_2 D_1 \Lambda_2$. Thus, the complex amplitude is introduced by the Cartesian coordinate

$$A_j(T_1) = \frac{1}{2} (W_j - iR_j) e^{iv_j} (j = 1, 2) \quad (31)$$

where $W_j = \Lambda_j \cos\eta_j$, $R_j = \Lambda_j \sin\eta_j$, and v_j are chosen such that the solutions are not explicitly dependent on the time.

For the first primary resonance (i.e., the first linear frequency is directly excited), $v_1 = 2\sigma_0 T_1 - \sigma_1 T_1$ and $v_2 = \sigma_0 T_1$. As a result, the Cartesian form of Eq. (23) can be expressed as

$$DW_1 = \text{Re}(\Xi_{11})W_1 + \text{Im}(\Xi_{11})R_1 - \sigma_0 R_1 - \frac{1}{2} \text{Im}(\Xi_{12})(-W_1 R_2 + R_1 W_2) \quad (32a)$$

$$DR_1 = \sigma_0 W_1 - \text{Im}(\Xi_{11})W_1 + \text{Re}(\Xi_{11})R_1 - \frac{1}{2} \text{Im}(\Xi_{12})(W_1 W_2 + R_1 R_2) - 2\text{Im}(\Xi_{13})G_1 \quad (32b)$$

$$DW_2 = \text{Re}(\Xi_{21})W_2 + \text{Im}(\Xi_{21})R_2 - (2\sigma_0 - \sigma_1)R_2 + \text{Im}(\Xi_{22})W_1 R_1 \quad (32c)$$

$$DR_2 = (2\sigma_0 - \sigma_1)W_2 - \text{Im}(\Xi_{21})W_2 + \text{Re}(\Xi_{21})R_2 - \frac{1}{2} \text{Im}(\Xi_{22})(W_1^2 - R_1^2) \quad (32d)$$

The disturbance equation of Eq. (32) could be expressed as:

$$(D\Delta W_1 \ D\Delta R_1 \ D\Delta W_2 \ D\Delta R_2)^T = \mathbf{J}(\Delta W_1 \ \Delta R_1 \ \Delta W_2 \ \Delta R_2)^T \quad (33)$$

where the superscript T denotes the transpose of each matrix and \mathbf{J} is the Jacobian matrix of the fix points determined by Eq. (25). If all the eigenvalues of \mathbf{J} have a negative real part, then the corresponding trivial solution is asymptotically stable [35].

3.4 Parametric study

A series of parametric studies are conducted to explore the dynamic behaviors of the internal-resonance-based BVEH in this section. Parameters of the BVEH are set as: $m_1 = 0.1\text{kg}$, $m_2 = 0.1\text{kg}$, $k_1 = 56\text{N/m}$, $k_2 = 50\text{N/m}$, $L = 0.05\text{m}$, $d = 0.0495\text{m}$, $c_1 = 0.002\text{Ns/m}$, $c_2 = 0.001\text{Ns/m}$, $L_e = 0.005\text{H}$, $R_e = 10\Omega$, $\Gamma = 0.5\text{Tm}$, and $p = 0.15\text{m/s}^2$. The linear natural frequencies are $\omega_1 = 2.3181\text{Hz}$, $\omega_2 = 4.6343\text{Hz}$, thus, the 2:1 internal resonance could be activated when the vibration frequency is appropriately selected. The two modes are $P_1 = 0.5499$, $P_2 = -1.8186$, and the corresponding detuning parameter σ_1 is -0.0128rad/s . In the amplitude-frequency response figures, the steady-state responses are presented in solid lines, while the unstable steady-state responses are illustrated in the dotted lines.

Figure 4 shows the amplitude-frequency response curves of X and I for different vibration amplitudes p . The typical double-jumping phenomenon is obtained for both X and I . Two separated multiple-valued ranges and two peaks are bending in two opposite directions, which could expand the harvesting bandwidth. Besides, it is seen that the unstable responses spring up with the increase of p , and it may induce more chaotic responses. In a word, both X and I amplitude could be enlarged with a greater p , as well as the bandwidth.

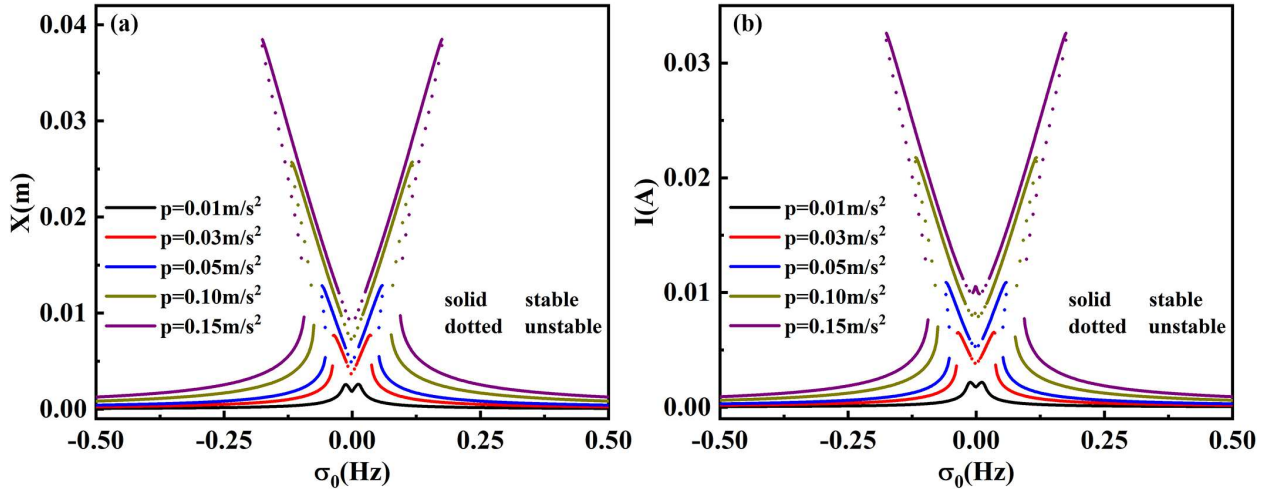


Fig. 4 Amplitude-frequency response curves for different p . (a) X , (b) I .

Figure 5 illustrates the amplitude-frequency response curves of X and I for different damping constant c_1 . It is seen that large c_1 leads to low-amplitude responses. Stable response is obtained in the entire vibration frequency range when $c_1 = 0.1\text{Ns/m}$. With the decrease of c_1 , the double-jumping phenomenon manifests, and the peak deviates further. Furthermore, the unstable ranges appear when c_1 is sufficiently small, and the bandwidth could also be expanded. c_1 has the opposite effects on the dynamic behaviors of the BVEH as p . The influence of c_2 on the amplitude-frequency response is investigated as well. A similar trend is obtained as the c_1 , thus it is not presented in this paper.

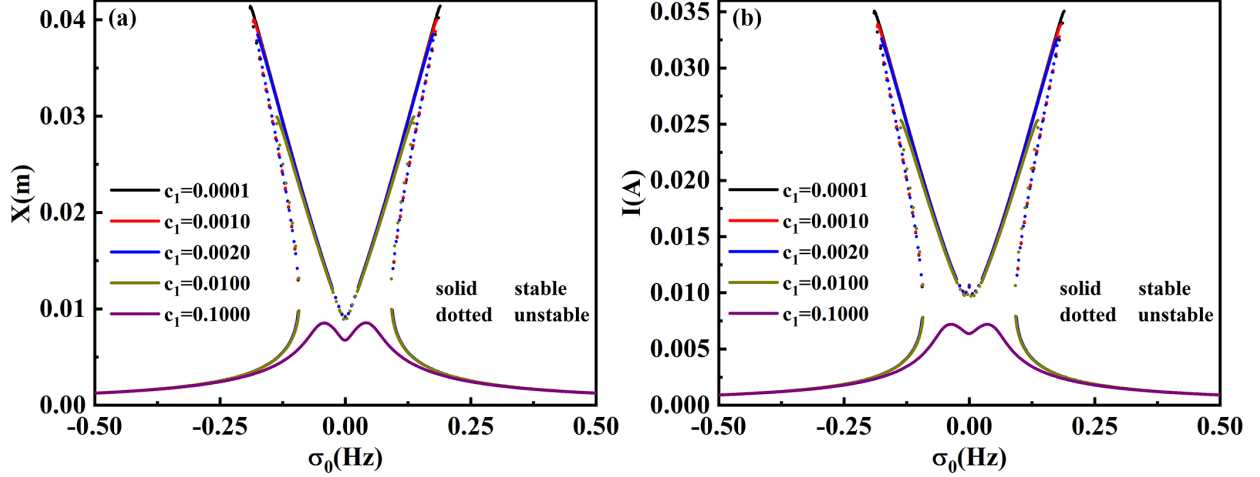


Fig. 5 Amplitude-frequency-response curves for different c_1 . (a) X , (b) I .

Figure 6 depicts the influence of Γ on the amplitude-frequency response of X and I . Though double-jumping phenomena appear in both X and I , different tendencies are obtained. For X , little Γ leads to greater displacement amplitude and wider bandwidth. For I , the “flower pattern” curves are obtained with different Γ as shown in figure 6(b). With a small Γ , the amplitude-frequency response curve is on the outermost side of the “flower pattern”, like the petals. With a greater Γ , the amplitude-frequency response curve is in the center of the “flower pattern”, like the stamens.

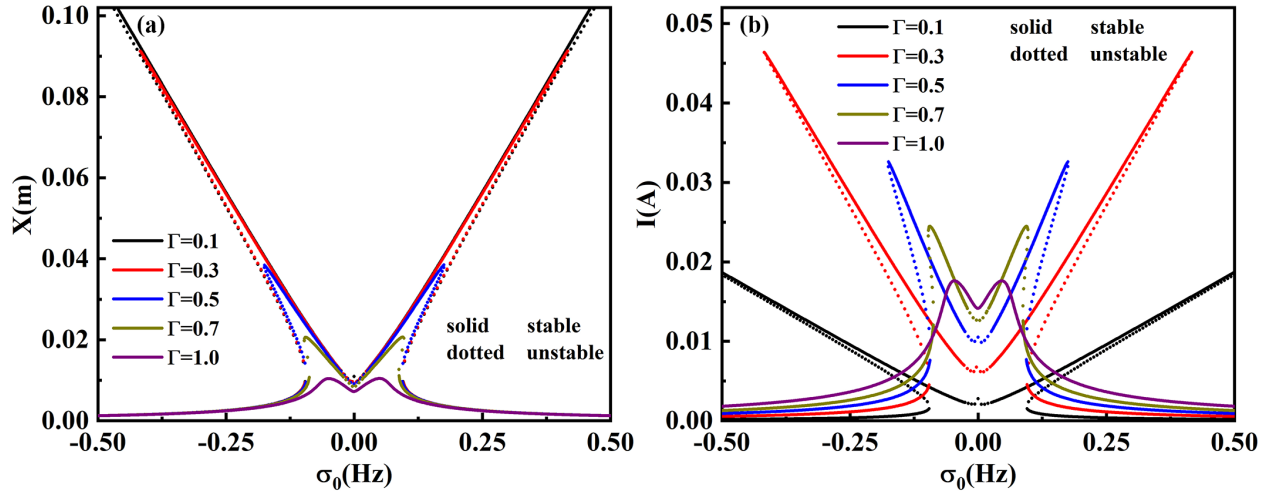


Fig. 6 Amplitude-frequency-response curves for different Γ . (a) X , (b) I .

The influence of L_e on the amplitude-frequency response of X and I is investigated as well, as shown in figure 7. Only two distinct curves are observed, though five different L_e are employed in this analysis. With a small L_e , i.e., $L_e < 0.05\text{H}$ in figure 7, no significant difference in amplitude-frequency response of X and I could be obtained. When L_e is up to 0.5H , the response changes a lot. The amplitude is greater, and the peak bends further in the opposite direction. It could be concluded that L_e is negligible when it is sufficiently small.

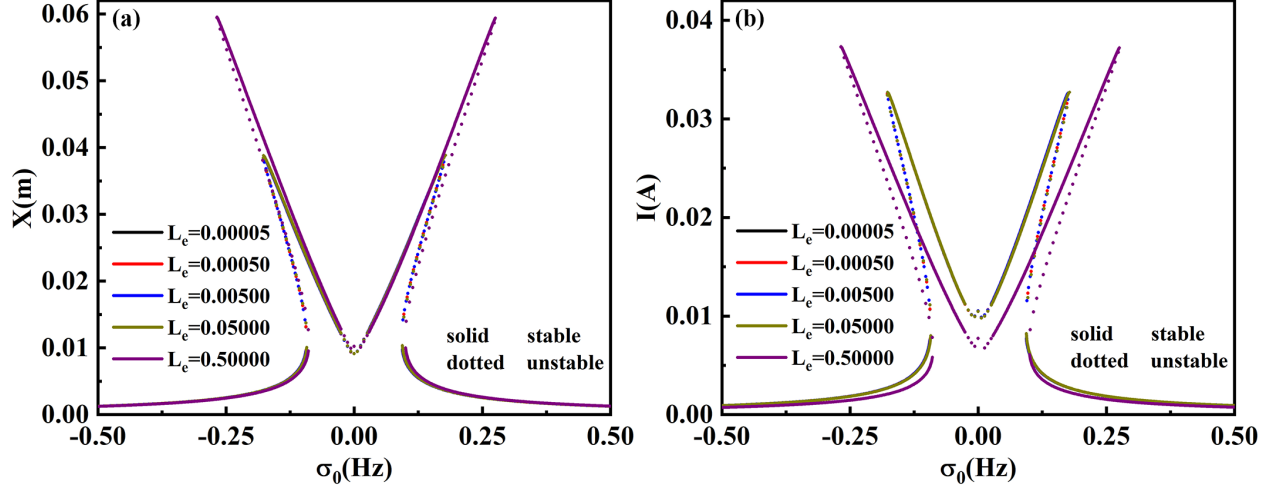


Fig. 7 Amplitude-frequency-response curves for different L_e . (a) X , (b) I .

Figure 8 shows the amplitude-frequency response curves of X and I for different resistor R_e . It is seen that R_e has a significant effect on the amplitude-frequency responses. Though the double-jumping phenomenon is ubiquitous, there exists a linear response when $R_e = 1$. In figure 8(b), it is apparent that the peak I appears with the completely tuned vibration frequency when $R_e = 1$. The amplitude drops rapidly under other vibration frequencies. With a greater R_e , two peaks appear immediately, and the bandwidth is enlarged due to the internal resonance characteristic.

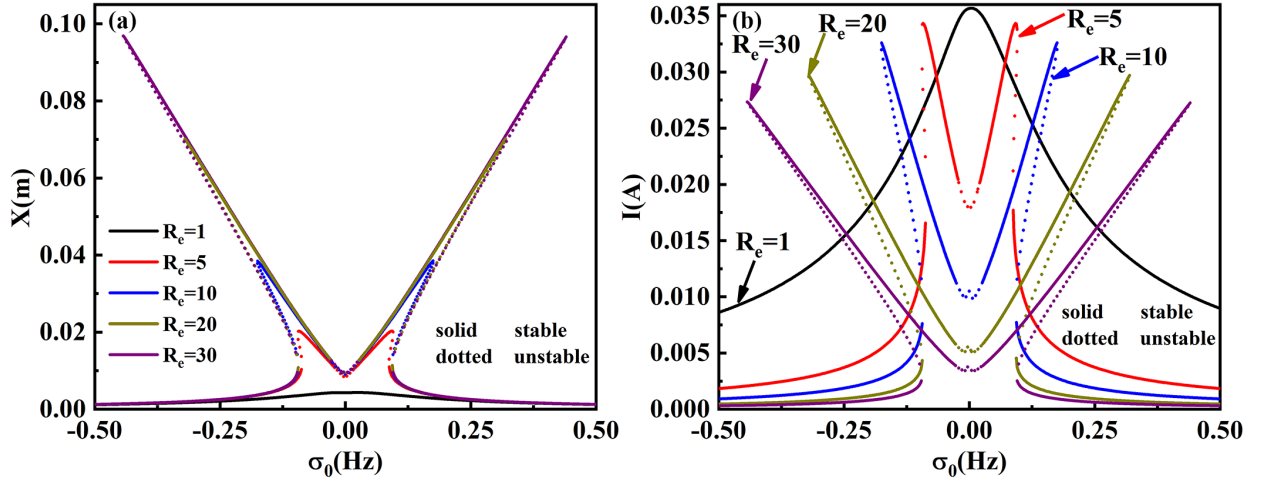


Fig. 8 Amplitude-frequency-response curves for different R_e . (a) X , (b) I .

Furthermore, numerical simulations under swept vibration excitation are investigated as well to verify the accuracy of the steady-state responses obtained by the multi-scale method. Both the forward sweep and backward sweep simulations are presented in figure 9. It is seen that the double-jumping phenomenon appears in the BVEH, which could expand the harvesting bandwidth. Besides, the swept simulation results show great agreement with the analytical results, especially the forward sweep simulation, which demonstrates the accuracy of the analytical approach.

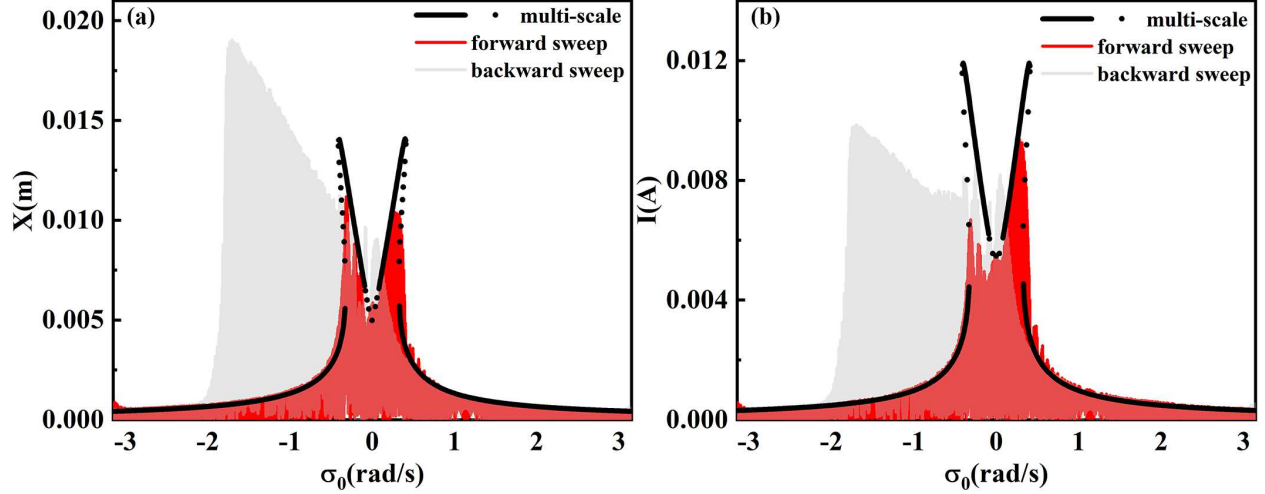


Fig. 9 Comparison of the amplitude-frequency response obtained by multi-scale method and sweep simulations when $p = 0.05\text{m/s}^2, c_1 = 0.0002\text{Ns/m}, c_2 = 0.0001\text{Ns/m}$. (a) X (b) I .

4 Numerical analysis

Numerical analyses are conducted in this section to further uncover the internal resonance characteristics of the BVEH. Both the small amplitude and large amplitude of the vibration are employed in the numerical analyses. Furthermore, the bistable nonlinearity of the BVEH is activated by increasing the vibration amplitude and the large-amplitude inter-well responses are obtained by the numerical analysis under large vibration amplitude.

4.1 Frequency spectrum and time-domain response

The dynamic responses of the BVEH at specific vibration frequencies are investigated to show the harmonic components in the response spectrums. A small vibration amplitude $p = 0.1\text{m/s}^2$ is employed at first, and the responses are presented in figure 10. It is seen that when the first mode is excited harmonically far away from the first linear natural frequency (i.e., $\Omega = 1.818\text{Hz}$, or 2.818Hz), only one distinct peak appears in the response spectrum, and the x amplitude is sufficiently small. However, when the first mode is excited harmonically at the first linear natural frequency (i.e., $\Omega = 2.318\text{Hz}$), an additional peak appears at nearly $2\omega_1$ (i.e., 4.682Hz), and the x amplitude is much greater. These results demonstrate that there exists strong mode coupling and energy exchanges between the first two modes when the 2:1 internal resonance is activated. The energy exchange between the first two modes obeys strict commensurate relation (i.e., in this case, 1:2), and the displacement amplitude could be increased which could enhance the harvesting performance.

Increase the vibration amplitude to $p = 0.5\text{m/s}^2$, some intriguing phenomena could be observed, as shown in figure 11. The response spectrums and time-domain responses for the BVEH when $\Omega = 1.818\text{Hz}$, or 2.818Hz are similar to those depicted in figure 10. Only one dominant peak appears at the same frequency as the vibration frequency, and the x amplitude is small. When $\Omega = \omega_1$, the nonlinear response changes a lot for the BVEH. Large-amplitude inter-well response is obtained, and the x amplitude increases several times. Furthermore, there is no distinct peak in the response spectrums. Instead, a multi-frequency response is obtained and the energy transfers to different modes, which leads to chaotic inter-well response. Figure 12 shows the phase portraits and the Poincare maps when $\Omega = 1.818, 2.318, \text{ and } 2.818\text{Hz}$, respectively.

The period-1 intra-well response is obtained for both $\Omega = 1.818\text{Hz}$ and $\Omega = 2.818\text{Hz}$, which contributes to low-efficiency. Differently, figure 12(b) presents a large-amplitude chaotic inter-well response. Two strange attractors at the two equilibria are observed, and plenty of irregular dispersed points are depicted in the Poincare map. m_1 oscillates around the two equilibria in a disordered way but with a clear boundary. The displacement amplitude increases multiple times compared with the intra-well responses, which has a positive impact on the energy harvesting performance of the BVEH.

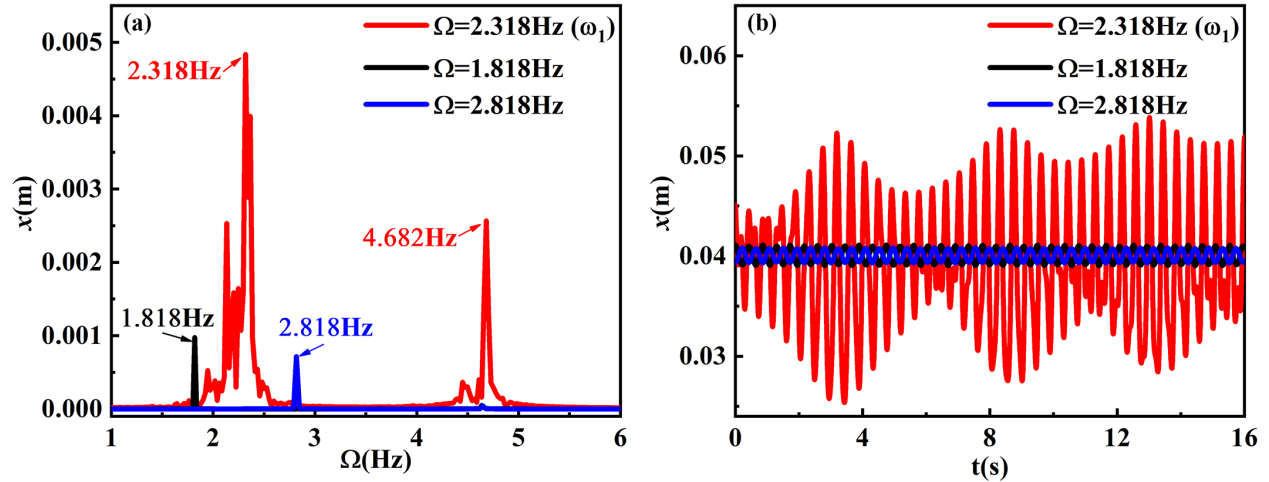


Fig. 10 (a)Response spectrum and (b) time trajectories with different vibration frequencies when $p = 0.15\text{m/s}^2$.

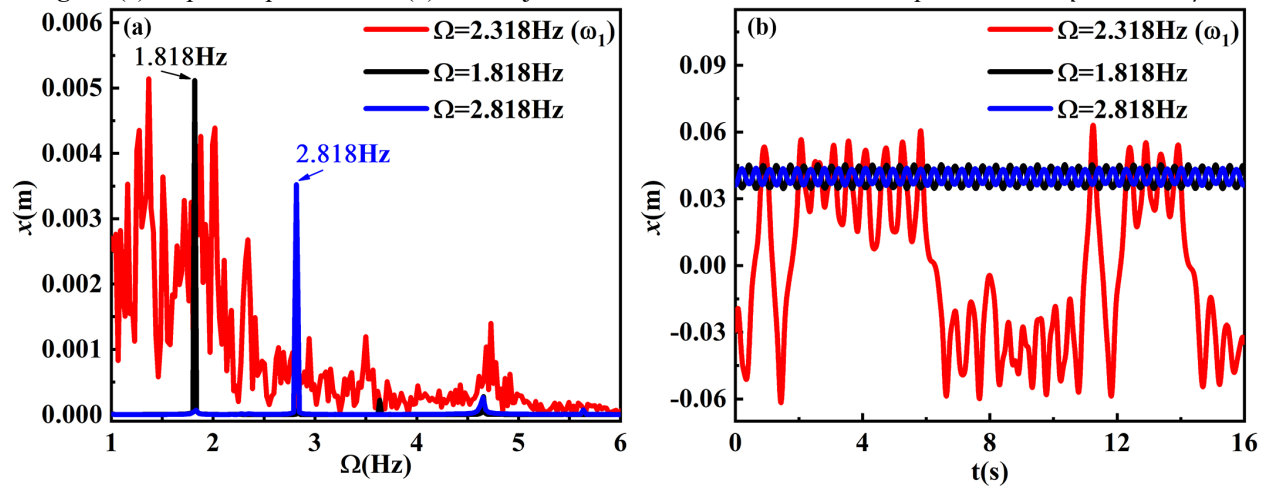


Fig. 11 (a)Response spectrum and (b) time trajectories with different vibration frequencies when $p = 0.5\text{m/s}^2$.

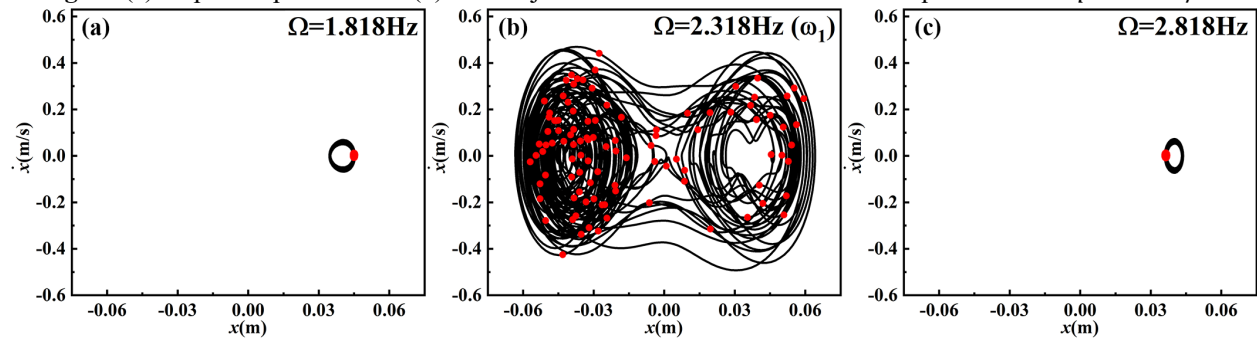


Fig. 12 Phase portraits and Poincare maps for the BVEH under different vibration frequencies. (a) $\Omega = 1.818\text{Hz}$, (b) $\Omega = 2.318\text{Hz}$, and (c) $\Omega = 2.818\text{Hz}$.

4.2 Bifurcation and basin-of-attraction

To develop the insights into the nonlinear dynamic responses, the bifurcation diagrams of the BVEH under specific vibration frequencies versus p are investigated, shown in figure 13. $c_1 = 0.0002\text{Ns/m}$ and $c_2 = 0.0001\text{Ns/m}$ are employed. It is seen that greater p might lead to inter-well responses when $\Omega = 1.818$ and 2.318 Hz. And the vibration amplitude needed when $\Omega = 2.318$ Hz is smaller, which demonstrates the internal resonance could increase the occurring probability for the large-amplitude inter-well responses. Besides, the inter-well responses could not be activated for the BVEH under a higher off-resonance vibration frequency, i.e., $\Omega = 2.818\text{Hz}$.

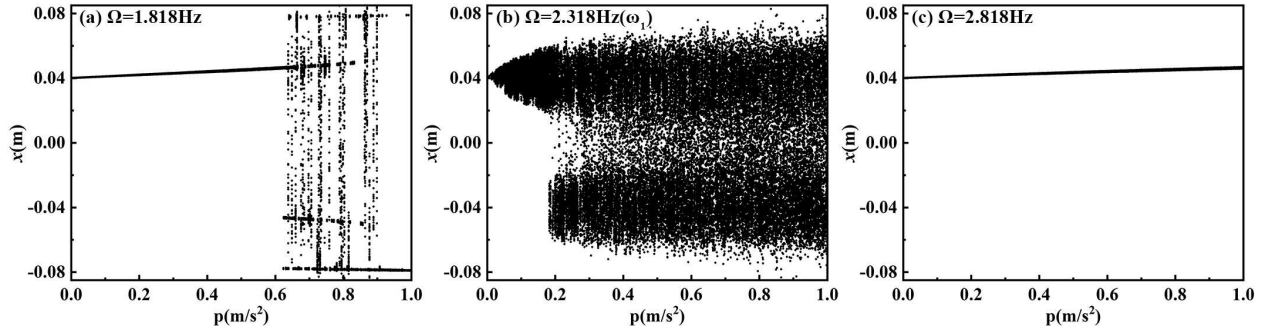


Fig. 13 Bifurcation diagrams of x displacement with the increase of vibration amplitude.

The basin-of-attraction maps of the BVEH are explored to quantitatively investigate the inter-well response occurring probability increment by the internal resonance. $p = 0.5\text{m/s}^2$, $c_1 = 0.0002\text{Ns/m}$ and $c_2 = 0.0001\text{Ns/m}$ are employed. Figure 14 shows the basin-of-attraction maps under specific vibration frequencies, i.e., $\Omega = 1.818$, 2.318 , and 2.818Hz . The red, yellow, and blue squares in this figure represent different initial conditions of m_1 , from where m_1 could realize period-1 inter-well, chaotic inter-well, and intra-well oscillation, respectively. Extremely different phenomena are depicted in figure 14. It is seen that the inter-well responses could not be activated when $\Omega = 2.818\text{Hz}$ no matter what the initial conditions the m_1 are chosen, and a complete blue-banded region is observed in figure 14(c). When $\Omega = 1.818\text{Hz}$, the period-1 and chaotic inter-well responses emerge with the occurring probabilities 8.76% and 0.61%. The intra-well response dominates with the occurring probability 90.62%. Thus, the BVEH might be inefficient when excited under an off-resonant vibration frequency. Furthermore, the chaotic inter-well response is ubiquitous when the BVEH is excited by a vibration frequency the same as the first linear natural frequency. The occurring probability of the chaotic inter-well response is 56.74%, which might improve the harvesting performance significantly.

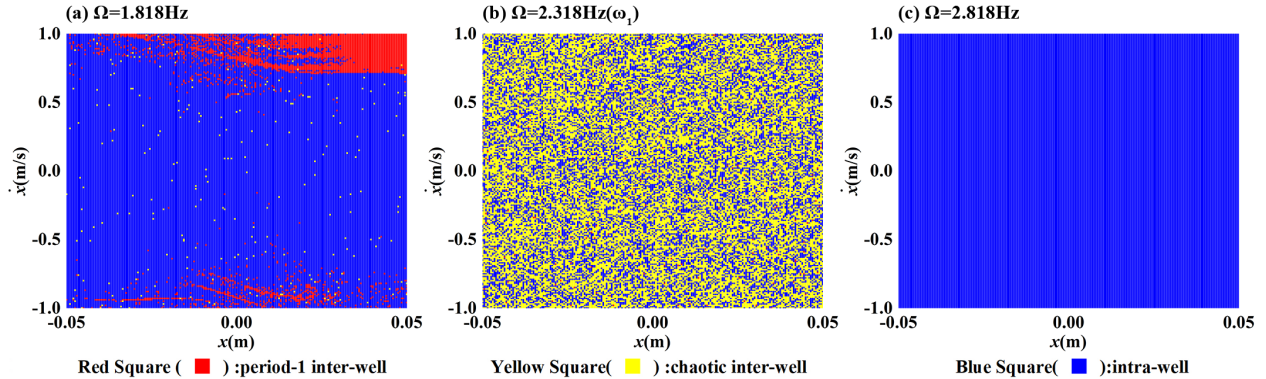


Fig. 14 Basin-of-attraction maps of the BVEH (a) $\Omega = 1.818\text{Hz}$, (b) $\Omega = 2.318\text{Hz}$, and (c) $\Omega = 2.818\text{Hz}$.

5 Conclusion

This paper explores the application of 2:1 internal resonance in bistable vibration energy harvester (BVEH). The BVEH combines with an inclined-spring-based bistable oscillator, an auxiliary oscillator, a linear track wound by coils, and the coils are connected with an electrical resistor. Two linear natural frequencies are tuned to meet the nearly commensurate ratio, i.e., 1:2. Thus, the 2:1 internal resonance could be activated when the first mode is directly excited. Amplitude-frequency responses under small vibration amplitudes are derived by the multi-scale method. Besides, the numerical method is employed to investigate the time-domain responses, frequency spectrums, bifurcation behaviors, and the basin-of-attraction maps of the BVEH. Intriguing nonlinear phenomena are revealed, and internal resonance has been proved to increase the occurring probability for the BVEH of exhibiting large-amplitude inter-well responses. The specific conclusions are:

- (1) The double-jumping phenomenon could be obtained in all the amplitude-frequency curves, two peaks bend in opposite directions, which expands the bandwidth of the BVEH. Among them, an intriguing “flower pattern” amplitude-frequency curve is observed. With a small resistor, the BVEH exhibits linear behavior, and the peak appears at the completely tuned vibration frequency.
- (2) The frequency spectrums are presented to show the mode coupling and energy exchanges between the first two modes. The x and I amplitude of the BVEH is much greater when excited at the first linear natural frequency than other off-resonance excitation frequencies. This result demonstrates that the harvesting performance of the BVEH could be enhanced by the internal resonance.
- (3) With small vibration amplitude, the BVEH exhibits intra-well responses, and the energy exchange between modes obeys strict commensurate relation, i.e., 2:1. Increase the vibration amplitude, and the inter-well responses are activated. The energy transfers to several low-frequency modes, and it does not obey the 2:1 ratio.
- (4) The bifurcation diagrams and basin-of-attraction maps demonstrate the BVEH is easy to realize inter-well responses when the internal resonance is activated under large vibration amplitude. Furthermore, the chaotic inter-well response dominates the nonlinear behaviors, and the occurring probability is 56.74%.

Compliance with ethical standards

1. Disclosure of potential conflicts of interest

This work is not used for any commercial business, and it has no conflicts of interest.

2. Research involving Human Participants and/or Animals

This work is about the mechanical engineering. This research doesn't involve any human participants or animals.

3. Informed consent

Only the authors listed in the manuscript are involved into this work. The submission of this research is agreed by all the authors listed in the manuscript, and is permitted by both the authors' affiliations.

Appendix: Experimental validation

An experimental prototype shown in figure 15 is employed to validate the governing equations of the BVEH. The experimental parameters are: $m_1 \approx 0.5\text{kg}$, $m_2 \approx 0.066\text{kg}$, $k_1 \approx 2000\text{N/m}$, $k_2 \approx 980\text{N/m}$, $L \approx 0.109\text{m}$, $d \approx 0.1025\text{m}$. Slowly swept base acceleration excitation from 1Hz to 8Hz at a rate of 0.025Hz/s is generated by the shaker, and two vibration excitation amplitudes are employed which are $p =$

1m/s^2 and $p = 3.53\text{m/s}^2$, respectively. The acceleration of m_1 is measured by the accelerometer, and the RMS accelerations are presented in figure 16. It is seen that the BVEH could only realize small-amplitude intra-well oscillations when $p = 1\text{m/s}^2$. However, the large-amplitude inter-well oscillations are obtained when a greater vibration excitation amplitude $p = 3.53\text{m/s}^2$ is employed. The RMS acceleration amplitude increases multi-times when the BVEH realizes inter-well oscillations. Besides, it could be concluded that the experimental results are similar to the numerical results. The bandwidth and RMS acceleration amplitude of the experimental and numerical results are in great agreement. In conclusion, the accuracy of the governing equations are validated, the results presented in this paper are reliable.

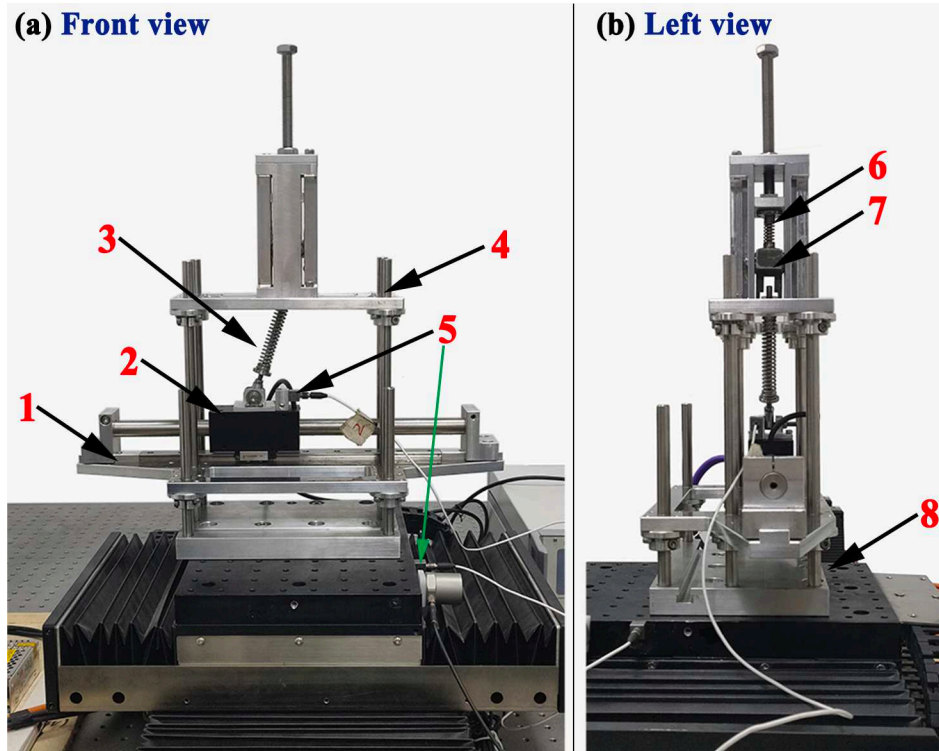


Fig. 15 Experimental prototype. 1-linear track; 2-embedded magnet m_1 ; 3-inclined spring k_1 ; 4-frame; 5-accelerators; 6-linear spring k_2 ; 7-auxiliary mass block m_2 ; 8-shaker.

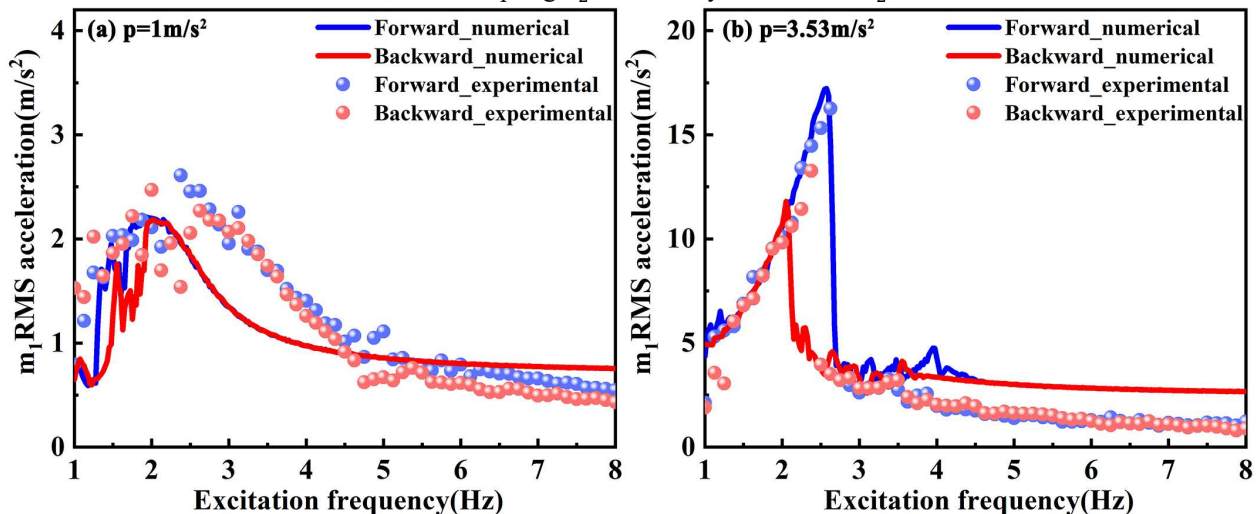


Fig. 16 Experimental validation.

References

- [1] Harne, R.L., Wang, K.W.: *Harnessing Bistable Structural Dynamics (For Vibration Control, Energy Harvesting and Sensing)*. Wiley, West Sussex (2017)
- [2] Zhang, J., Yang, K., Li, R.: A bistable nonlinear electromagnetic actuator with elastic boundary for actuation performance improvement. *Nonlinear Dynam.* **100**, 3575-3596 (2020)
- [3] Fang, H., Wang, K.W.: Piezoelectric vibration-driven locomotion systems—exploiting resonance and bistable dynamics. *J. Sound Vib.* **391**, 153–169 (2017)
- [4] Maamer, B., Boughamoura, A., Fath El-Bab, A. M. R., Francis, L. A., Tounsi, F.: A review on design improvements and techniques for mechanical energy harvesting using piezoelectric and electromagnetic schemes. *Energ. Convers. Manage.* **199**, 111973 (2019)
- [5] Siddique, A. R. M., Mahmud, S., Heyst, B. V.: A comprehensive review on vibration based micro power generators using electromagnetic and piezoelectric transducer mechanisms. *Energ. Convers. Manage.* **106**, 728-747 (2015)
- [6] Yang, K., Wang, J., Yurchenko, D.: A double-beam piezo-magneto-elastic wind energy harvester for improving the galloping-based energy harvesting. *Appl. Phys. Lett.* **115**, 193901 (2019)
- [7] Nguyen, M. S., Yoon, Y.J., Kwon, O., Kim, P.: Lowering the potential barrier of a bistable energy harvester with mechanically rectified motion of an auxiliary magnet oscillator. *Appl. Phys. Lett.* **111**, 253905 (2017)
- [8] Zhou, Z., Qin, W., Du, W., Zhu, P., Liu, Q.: Improving energy harvesting from random excitation by nonlinear flexible bi-stable energy harvester with a variable potential energy function. *Mech. Syst. Signal Pr.* **115**, 162-172 (2019)
- [9] Leng, Y. G., Gao, Y. J., Tan, D., Fan, S. B., Lai, Z. H.: An elastic-support model for enhanced bistable piezoelectric energy harvesting from random vibrations. *J. Appl. Phys.* **117**, 064901 (2015)
- [10] Harne, R. L., Thota, M., Wang, K. W.: Bistable energy harvesting enhancement with an auxiliary linear oscillator. *Smart Mater. Struct.* **22**, 125028 (2013)
- [11] Mao, X.Y., Ding, H., Chen, L.-Q.: Steady-state response of a fluid-conveying pipe with 3:1 internal resonance in supercritical regime. *Nonlinear Dynam.* **86**, 795-809 (2016)
- [12] Alfossail, F. K., Younis, M. I.: Two-to-one internal resonance of an inclined marine riser under harmonic excitations. *Nonlinear Dynam.* **95**, 1301-1321 (2018)
- [13] Alfossail, F. K., Hajjaj, A. Z., Younis, M. I.: Theoretical and Experimental Investigation of Two-to-One Internal Resonance in MEMS Arch Resonators. *J. Comput. Nonlin. Dyn.* **14**, 011001 (2019)
- [14] Guo, X., Jiang, P., Yan, W., Lai, S.-K., Zhang, W.: Internal Resonance Responses of Rectangular Cross-Ply Composite Plates with Graphene Skins. *Int. J. Struct. Stab. Dy.* **19**, 1950057 (2019)
- [15] Nazemnezhad, R., Mahoori, R., Samadzadeh, A.: Surface energy effect on nonlinear free axial vibration and internal resonances of nanoscale rods. *Eur. J. Mech. A-Solid.* **77**, 103784 (2019)
- [16] Inoue, T., Ishida, Y.: Chaotic Vibration and Internal Resonance Phenomena in Rotor Systems. *J. Vib. Acoust.* **128**, 156-169 (2005)
- [17] Hacker, E., Gottlieb, O.: Application of reconstitution multiple scale asymptotics for a two-to-one internal resonance in Magnetic Resonance Force Microscopy. *Int. J. Nonlin. Mech.* **94**, 174-199 (2017)

- [18] Wang, X., Huan, R., Zhu, W., Pu, D., Wei, X.: Frequency locking in the internal resonance of two electrostatically coupled micro-resonators with frequency ratio 1:3. *Mech. Syst. Signal Pr.* **146**, 106981 (2021)
- [19] Kirkendall, C. R., Kwon, J. W.: Multistable internal resonance in electroelastic crystals with nonlinearly coupled modes. *Sci. Rep-UK.* **6**, 22897 (2016)
- [20] Sayed, M., Kamel, M.: 1:2 and 1:3 internal resonance active absorber for non-linear vibrating system. *Appl. Math. Model.* **36**, 310-332 (2012)
- [21] Karimpour, H., Eftekhari, M.: Exploiting double jumping phenomenon for broadening bandwidth of an energy harvesting device. *Mech. Syst. Signal Pr.* **139**, 106614 (2020)
- [22] Chen, L., Jiang, W.: A piezoelectric energy harvester based on internal resonance. *Acta Mech. Sinica-Proc.* **31**, 223-228 (2015)
- [23] Xu, J., Tang, J.: Multi-directional energy harvesting by piezoelectric cantilever-pendulum with internal resonance. *Appl. Phys. Lett.* **107**, 213902 (2015)
- [24] Rocha, R. T., Balthazar, J. M., Tusset, A. M., Piccirillo, V., Felix, J. L. P.: Nonlinear piezoelectric vibration energy harvesting from a portal frame with two-to-one internal resonance. *Meccanica* **52**, 2583-2602 (2017)
- [25] Garg, A., Dwivedy, S. K.: Nonlinear dynamics of parametrically excited piezoelectric energy harvester with 1:3 internal resonance. *Int. J. Nonlin. Mech.* **111**, 82-94 (2019)
- [26] Jiang, W.A., Chen, L.Q., Ding, H.: Internal resonance in axially loaded beam energy harvesters with an oscillator to enhance the bandwidth. *Nonlinear Dynam.* **85**, 2507-2520 (2016)
- [27] Cao, D. X., Leadenham, S., Erturk, A.: Internal resonance for nonlinear vibration energy harvesting. *Eur. Phys. J-Spec. Top.* **224**, 2867-2880 (2015)
- [28] Yang, W., Towfighian, S.: A hybrid nonlinear vibration energy harvester. *Mech. Syst. Signal Pr.* **90**, 317-333 (2017)
- [29] Chen, L.Q., Jiang, W. A.: Internal Resonance Energy Harvesting. *J. Appl. Mech-T. ASME.* **82**, 031004 (2015)
- [30] Xiong, L., Tang, L., Mace, B. R.: Internal resonance with commensurability induced by an auxiliary oscillator for broadband energy harvesting. *Appl. Phys. Lett.* **108**, 203901 (2016)
- [31] Yang, W., Towfighian, S.: Internal resonance and low frequency vibration energy harvesting. *Smart Mater. Struct.* **26**, 095008 (2017)
- [32] Hou, S., Teng, Y.Y., Zhang, Y.-W., Zang, J.: Enhanced Energy Harvesting of a Nonlinear Energy Sink by Internal Resonance. *Int. J. Appl. Mech.* **11**, 1950100 (2020)
- [33] Lan, C., Qin, W., Deng, W.: Energy harvesting by dynamic instability and internal resonance for piezoelectric beam. *Appl. Phys. Lett.* **107**, 093902 (2015)
- [34] Nie, X., Tan, T., Yan, Z., Yan, Z., Hajj, M. R.: Broadband and high-efficient L-shaped piezoelectric energy harvester based on internal resonance. *Int. J. Mech. Sci.* **159**, 287-305 (2019)
- [35] Zhang, J., Li, X., Li, R., Dai, L., Wang, W., Yang, K.: Internal resonance of a two-degree-of-freedom tuned bistable electromagnetic actuator. *Chaos Soliton Fract.* **143**, 110612 (2021)

Figures

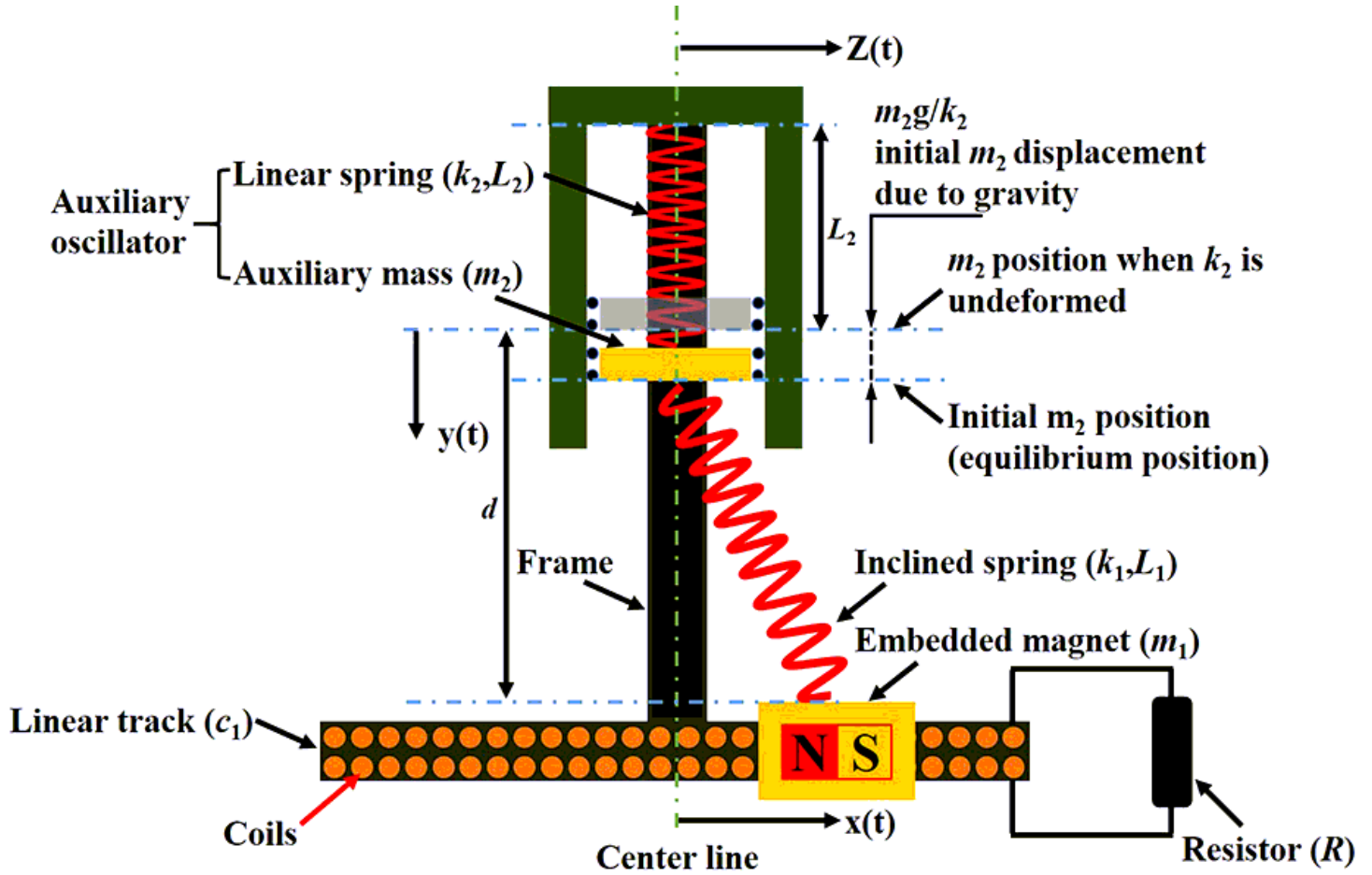


Figure 1

Schematic diagram of the BVEH (a)

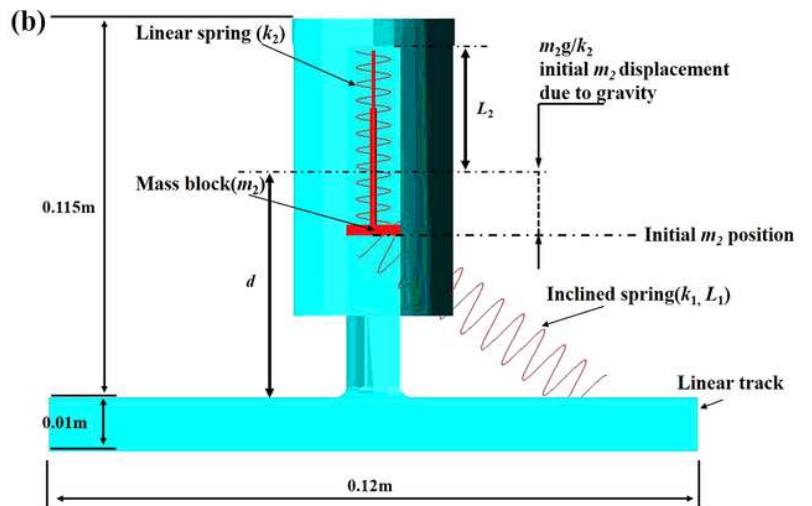
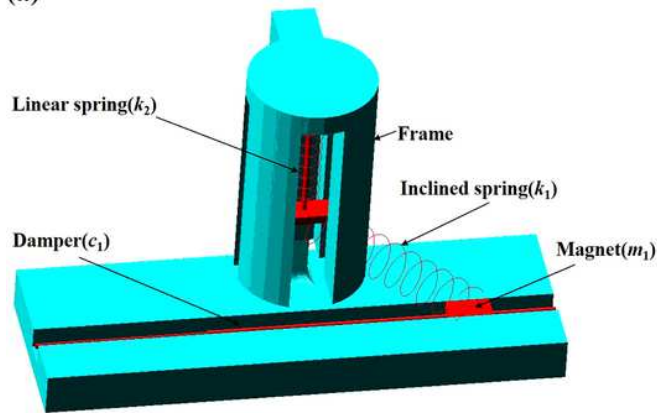


Figure 2

The 3D virtual prototype of the BVEH in Adams software. (a) Isometric graph; (b) planar graph.

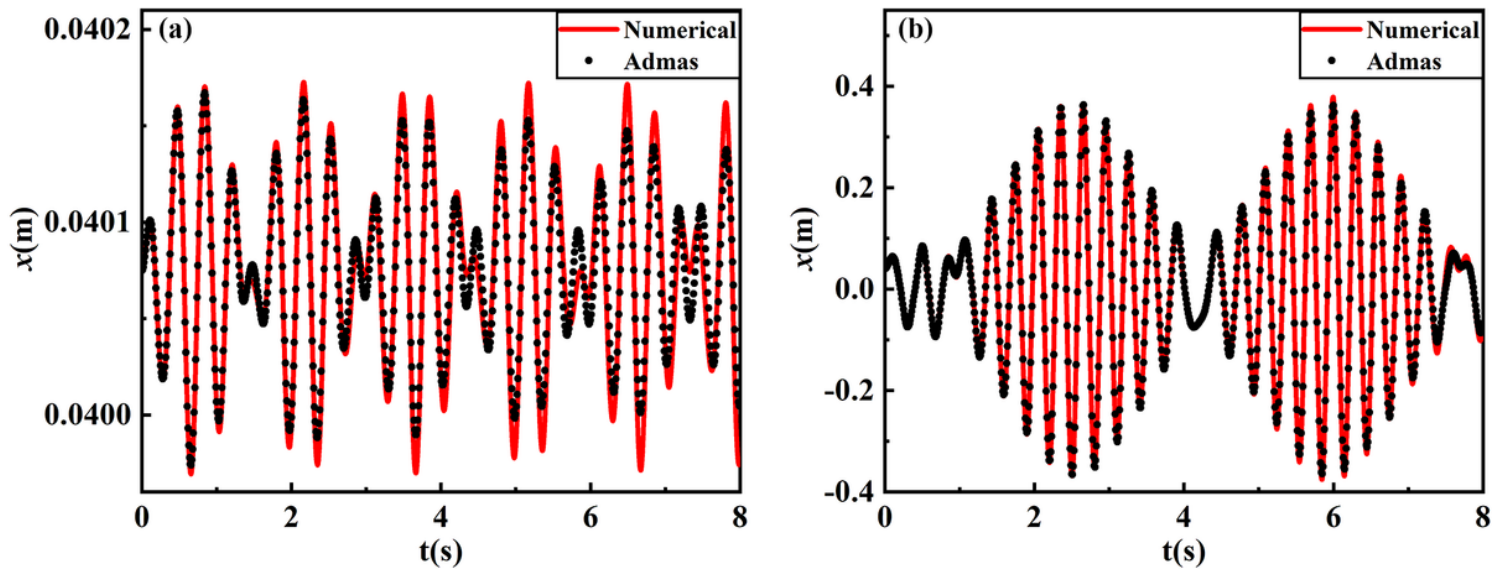


Figure 3

Comparison between the numerical method and the Adams. (a) $p=0.01\text{m/s}^2$; (b) $p=10\text{m/s}^2$.

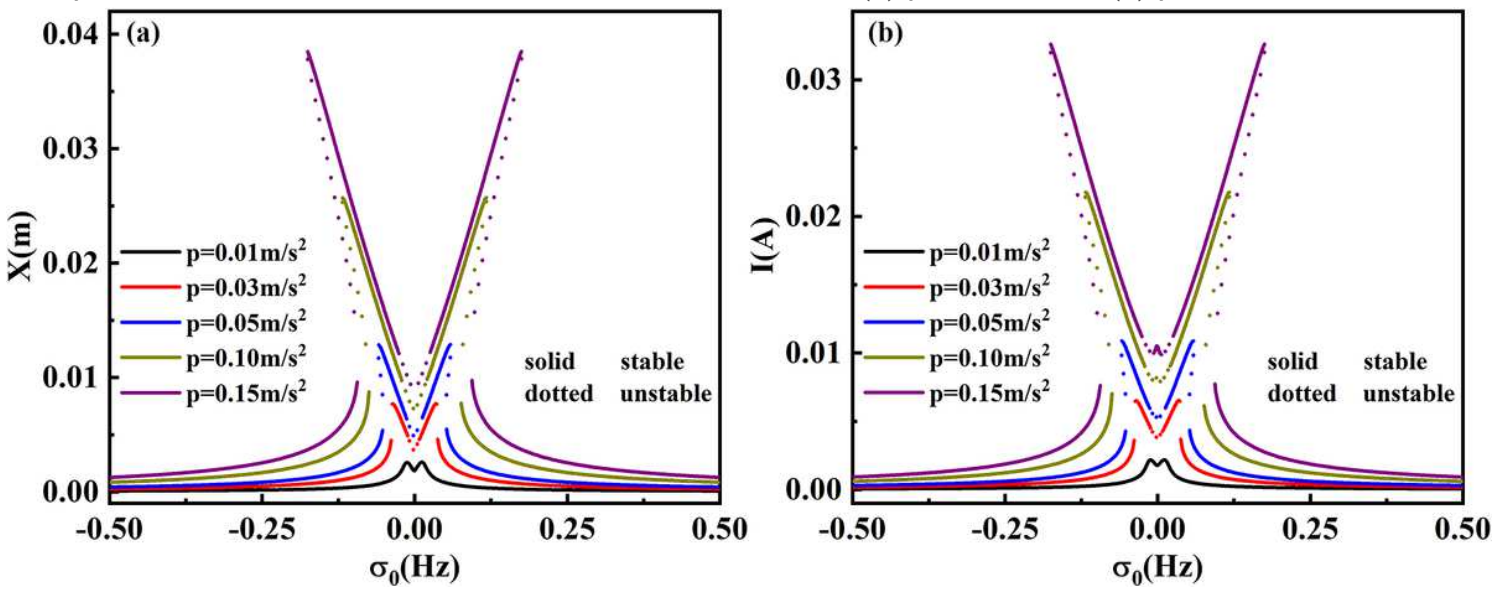


Figure 4

Amplitude-frequency response curves for different p . (a) X , (b) I .

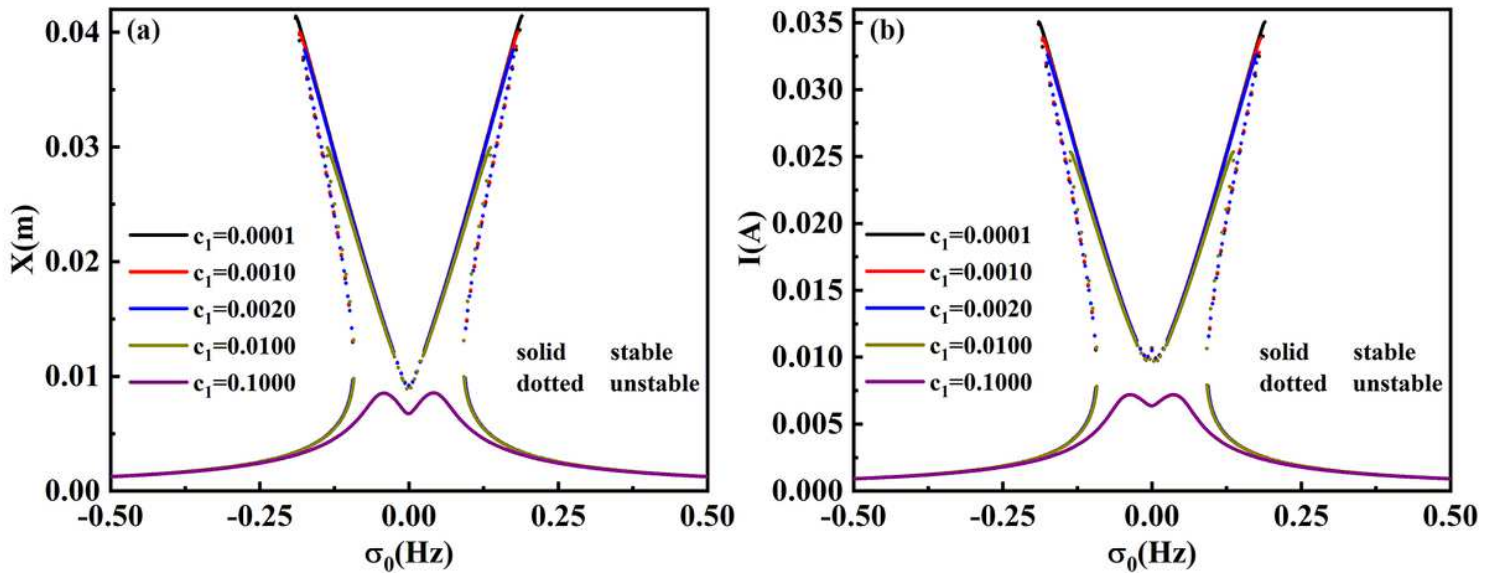


Figure 5

Amplitude-frequency-response curves for different c_1 . (a) X , (b) I .

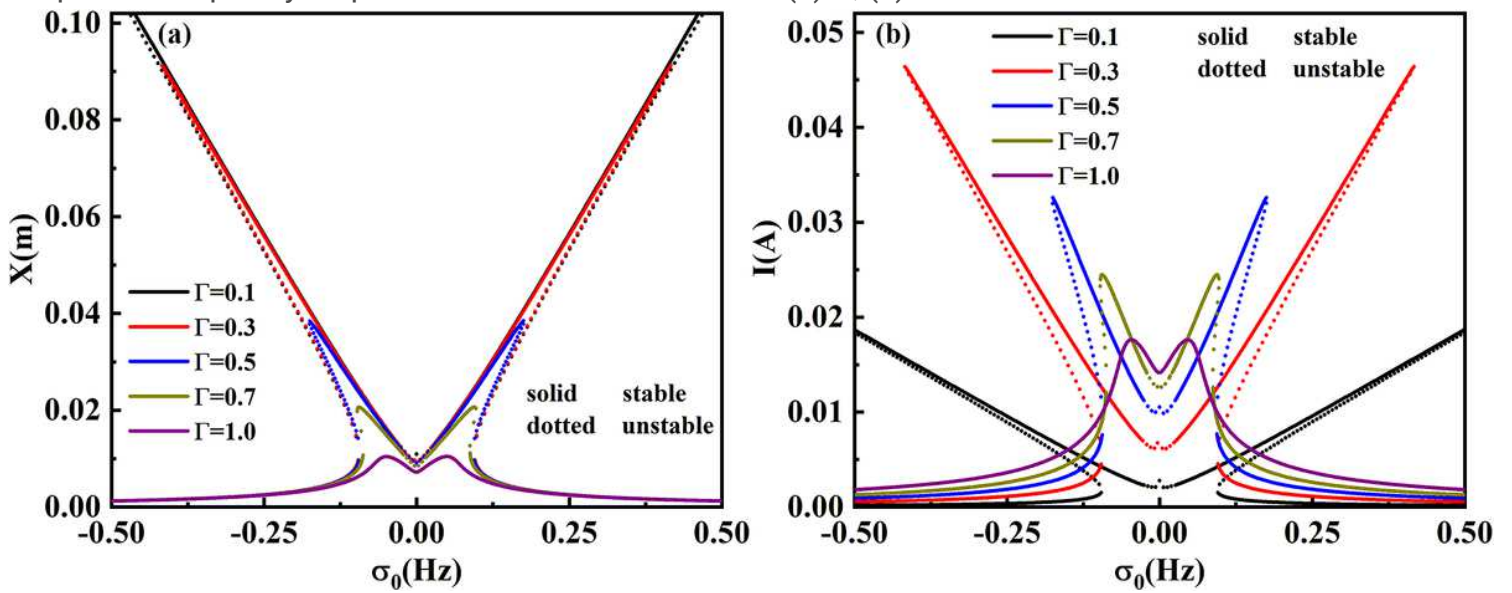


Figure 6

Amplitude-frequency-response curves for different Γ . (a) X , (b) I .

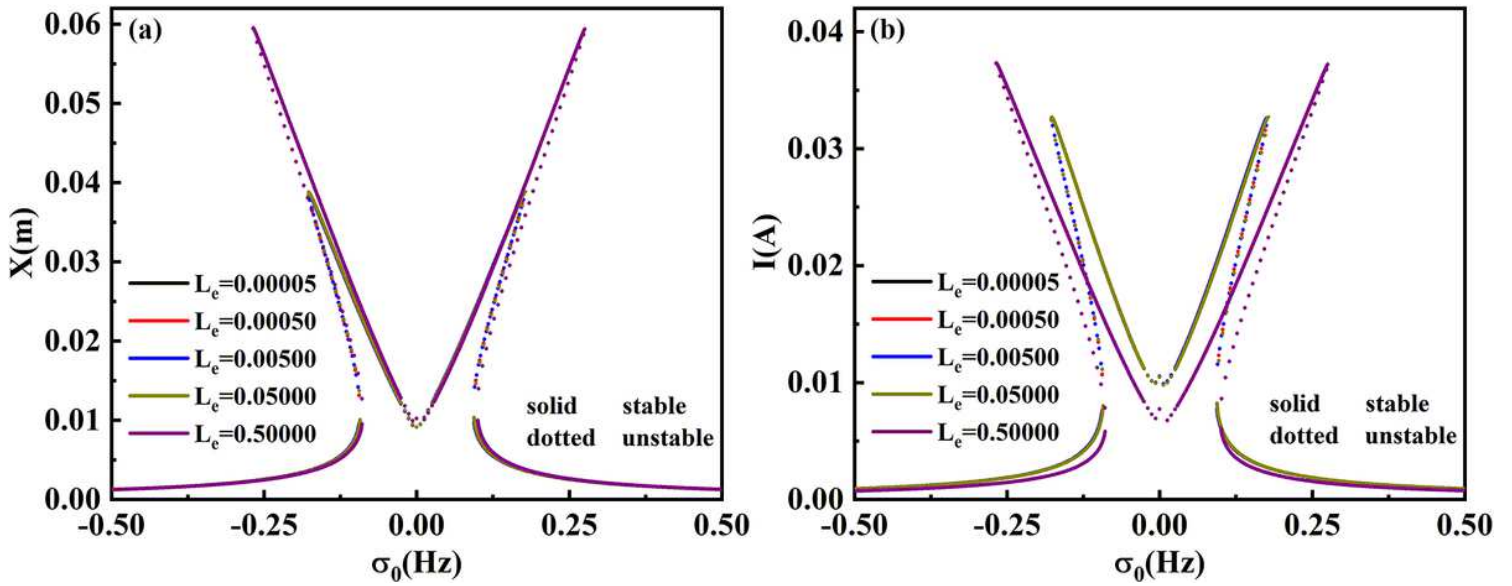


Figure 7

Amplitude-frequency-response curves for different L_e . (a) X , (b) I .

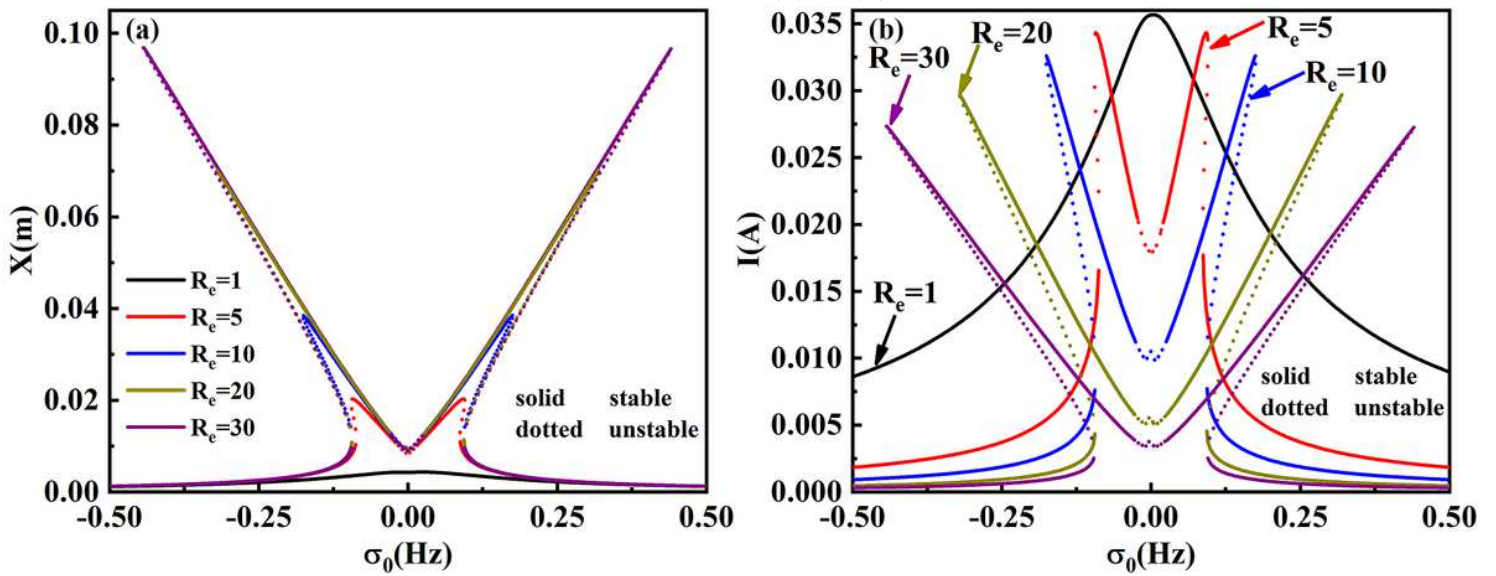


Figure 8

Amplitude-frequency-response curves for different R_e . (a) X , (b) I .

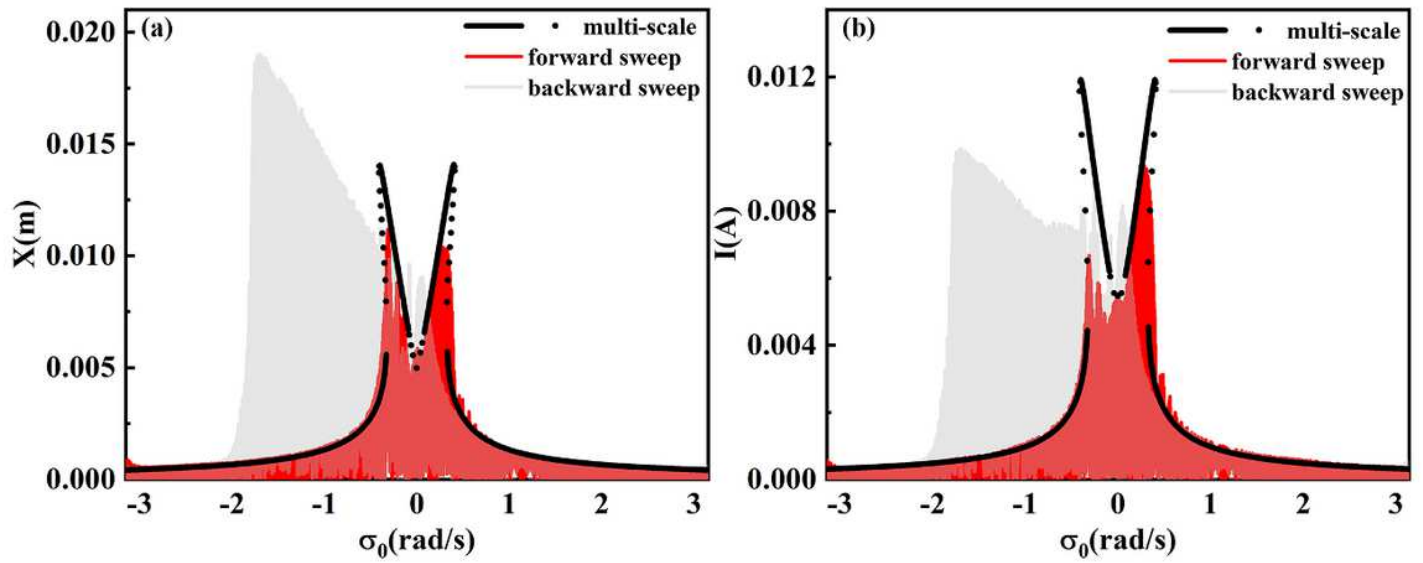


Figure 9

Comparison of the amplitude-frequency response obtained by multi-scale method and sweep simulations when $p=0.05\text{m/s}^2, c_1=0.0002\text{Ns/m}, c_2=0.0001\text{Ns/m}$. (a) X (b) I .

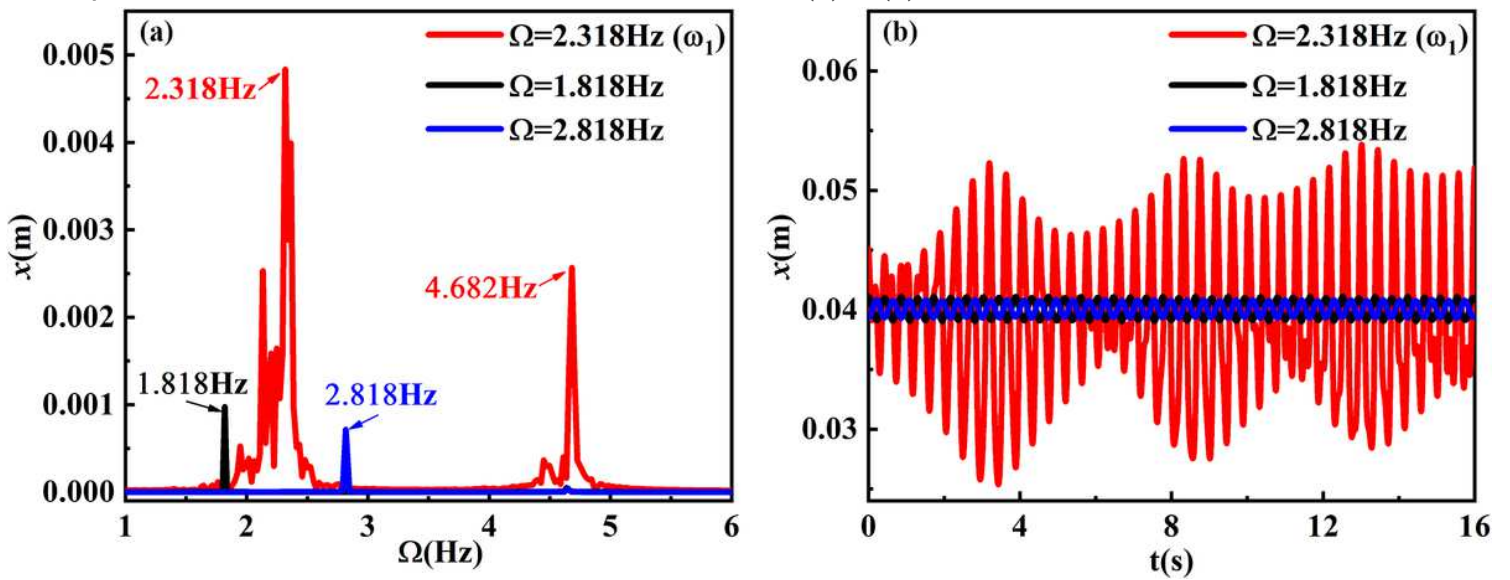


Figure 10

(a) Response spectrum and (b) time trajectories with different vibration frequencies when $p=0.15\text{m/s}^2$.

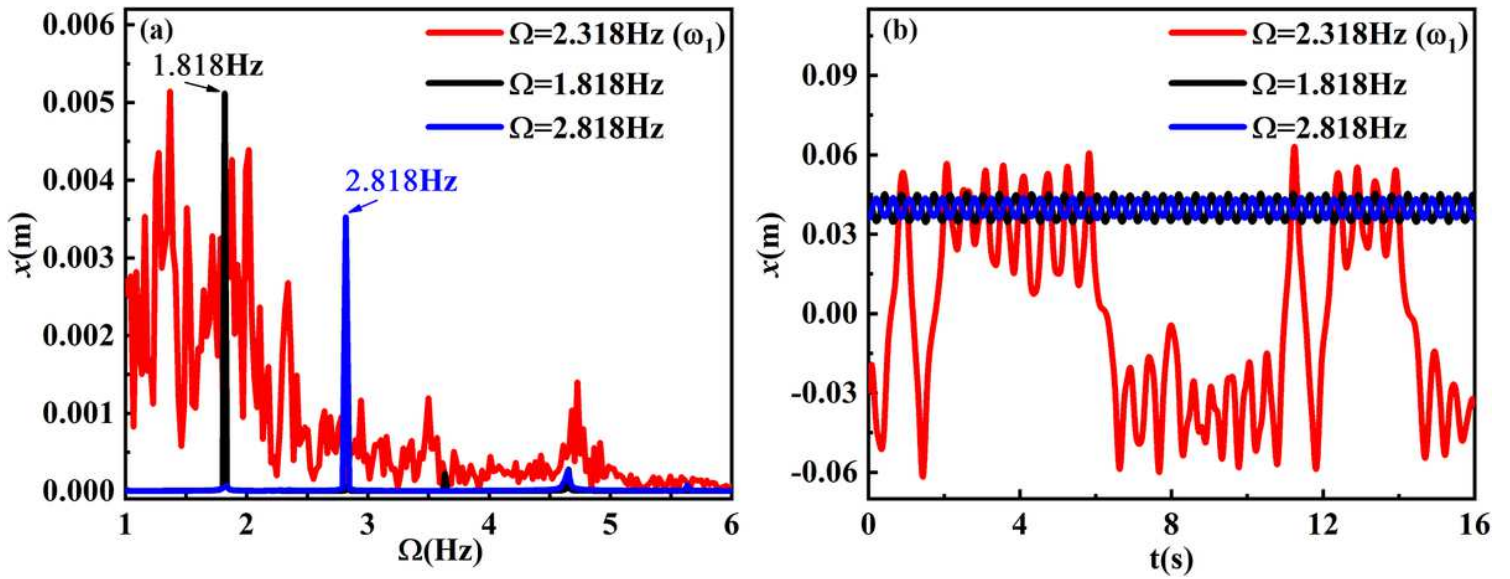


Figure 11

(a) Response spectrum and (b) time trajectories with different vibration frequencies when $p=0.5\text{m/s}^2$.

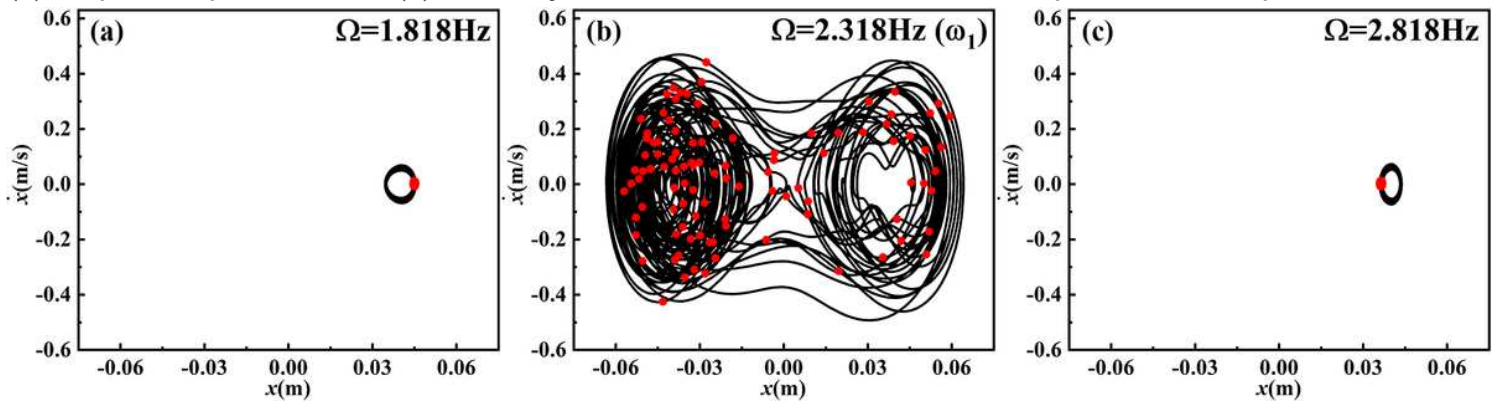


Figure 12

Phase portraits and Poincaré maps for the BVEH under different vibration frequencies. (a) $\Omega=1.818\text{Hz}$, (b) $\Omega=2.318\text{Hz}$, and (c) $\Omega=2.818\text{Hz}$.

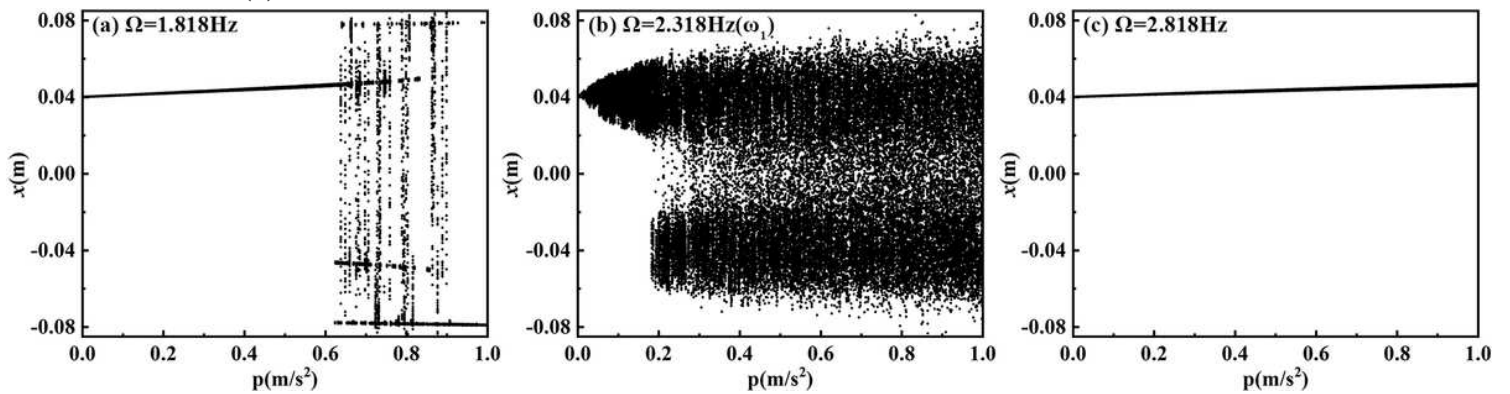


Figure 13

Bifurcation diagrams of x displacement with the increase of vibration amplitude.

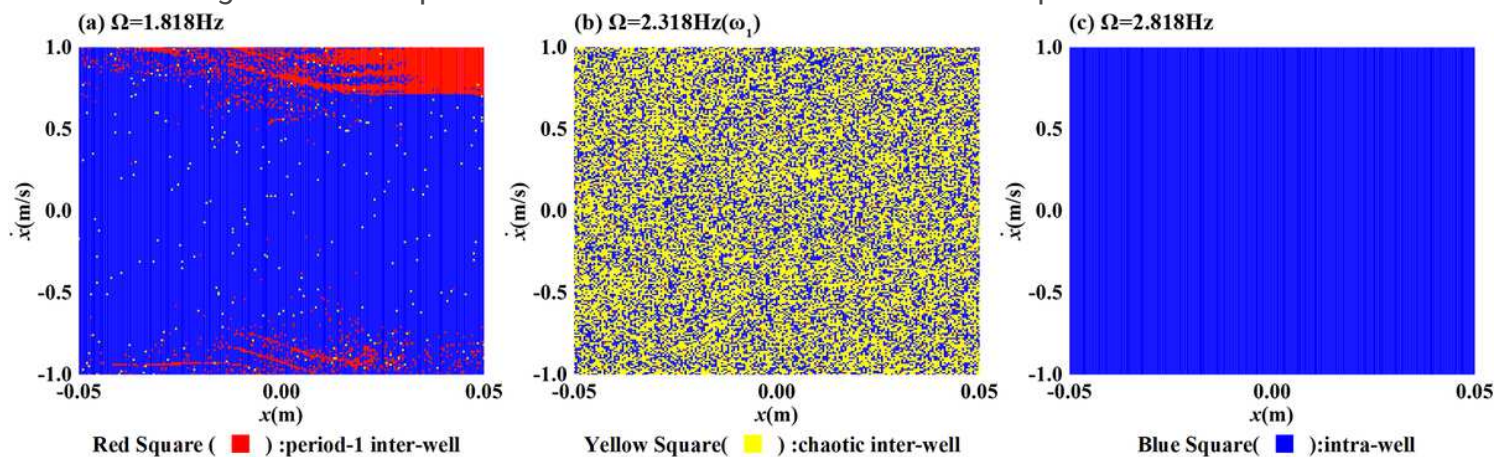


Figure 14

Basin-of-attraction maps of the BVEH (a) $\Omega=1.818\text{Hz}$, (b) $\Omega=2.318\text{Hz}$, and (c) $\Omega=2.818\text{Hz}$.

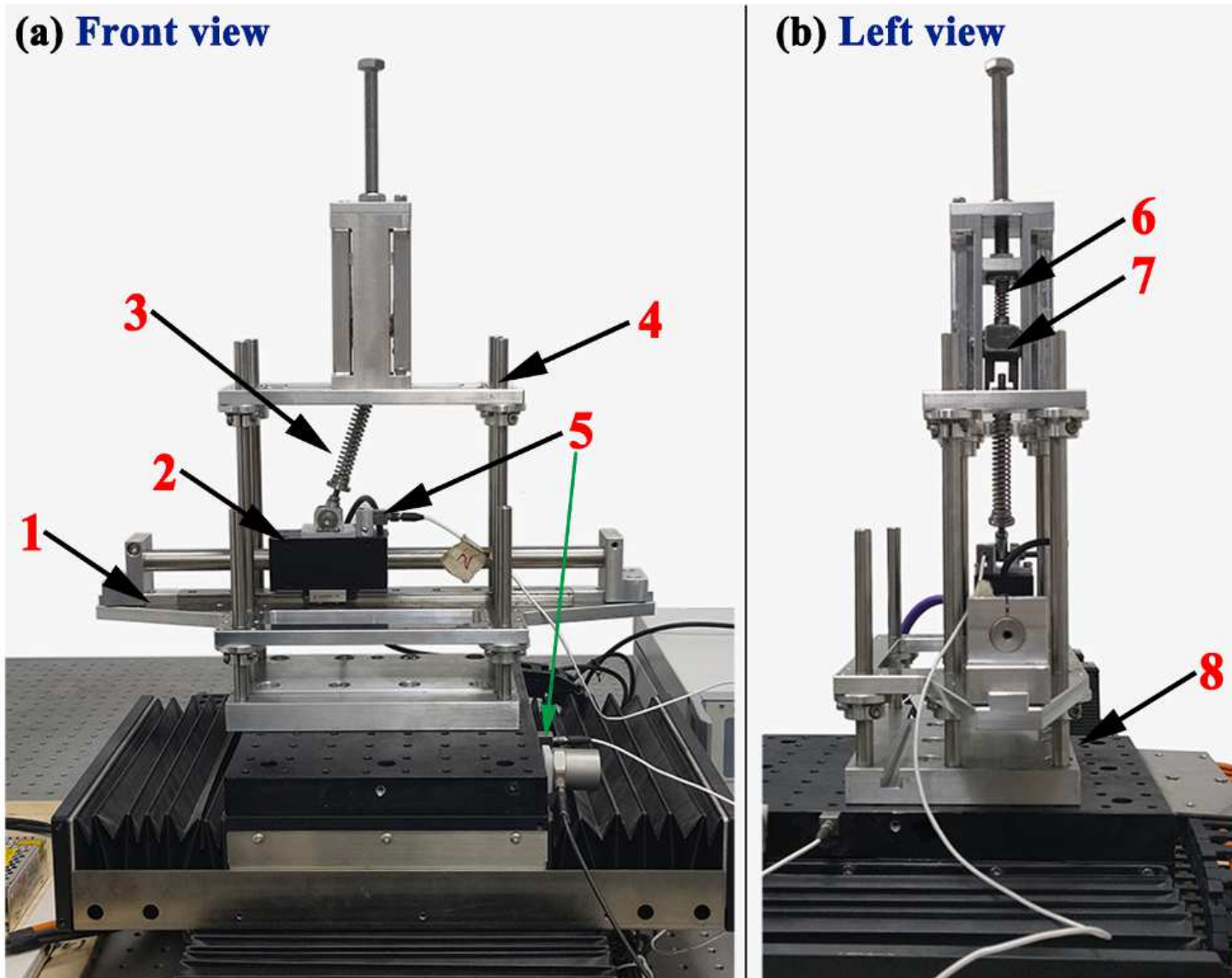


Figure 15

Experimental prototype. 1-linear track; 2-embedded magnet m_1 ; 3-inclined spring k_1 ; 4-frame; 5-accelerators; 6-linear spring k_2 ; 7-auxiliary mass block m_2 ; 8-shaker.

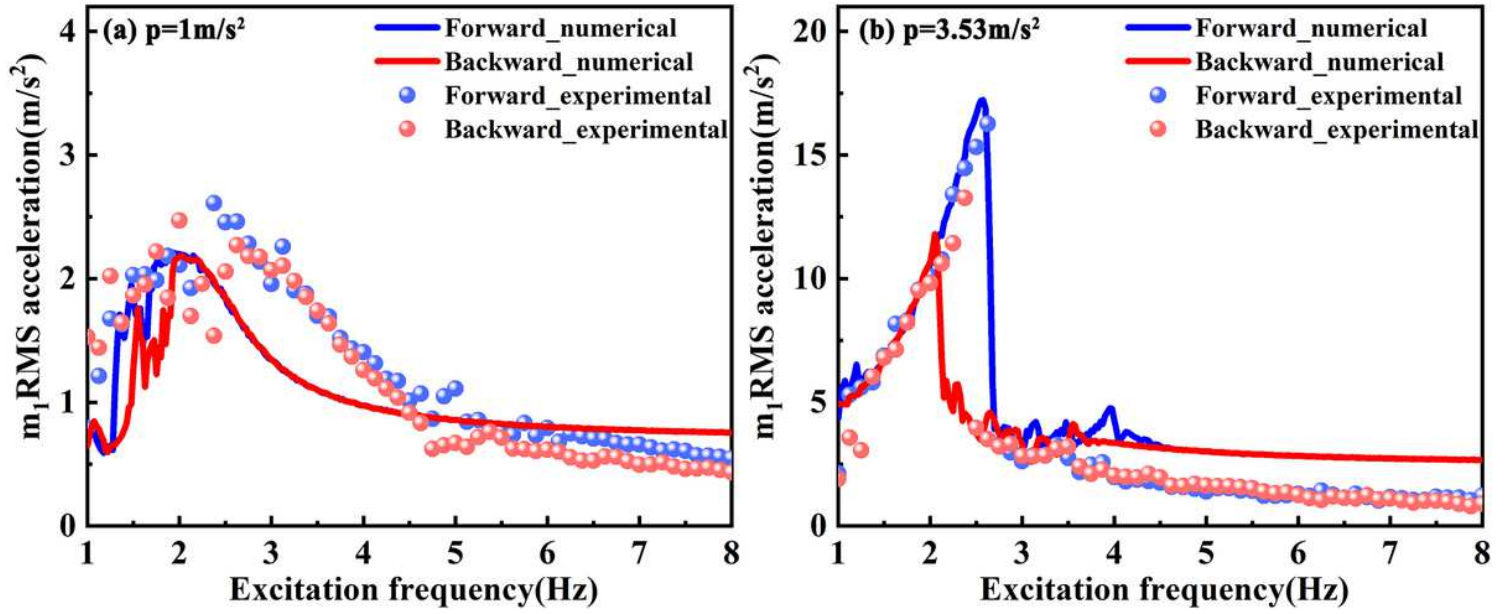


Figure 16

Experimental validation.